A Comparison of EAST Shock-Tube Radiation Measurements with a New Air Radiation Model

Christopher O. Johnston*
NASA Langley Research Center, Hampton, VA, 23681

This paper presents a comparison between the recent EAST shock tube radiation measurements (Grinstead et al., AIAA 2008-1244) and the HARA radiation model. The equilibrium and nonequilibrium radiation measurements are studied for conditions relevant to lunar-return shock-layers; specifically shock velocities ranging from 9 to 11 km/s at initial pressures of 0.1 and 0.3 Torr. The simulated shock-tube flow is assumed one-dimensional and is calculated using the LAURA code, while a detailed nonequilibrium radiation prediction is obtained in an uncoupled manner from the HARA code. The measured and predicted intensities are separated into several spectral ranges to isolate significant spectral features, mainly strong atomic line multiplets. The equations and physical data required for the prediction of these strong atomic lines are reviewed and their uncertainties identified. The 700 – 1020 nm wavelength range, which accounts for roughly 30% of the radiative flux to a peak-heating lunar return shock-layer, is studied in detail and the measurements and predictions are shown to agree within 15% in equilibrium. The ±1.5% uncertainty on the measured shock velocity is shown to cause up to a ±30% difference in the predicted radiation. This band of predictions contains the measured values in almost all cases. For the highly nonequilibrium 0.1 Torr cases, the nonequilibrium radiation peaks are under-predicted by about half. This under-prediction is considered acceptable when compared to the order-of-magnitude over-prediction obtained using a Boltzmann population of electronic states. The reasonable comparison in the nonequilibrium regions provides validation for both the non-Boltzmann modeling in HARA and the thermochemical nonequilibrium modeling in LAURA. The N_2^+(1-) and N_2(2+) molecular band systems are studied in the 290 – 480 nm wavelength range for both equilibrium and nonequilibrium regimes. The non-Boltzmann rate models for these systems, which have significant uncertainties, are tuned to improve the comparison with measurements.

Nomenclature

B_λ	=	Blackbody or Planck function written in terms of wavelength (erg/cm^3/s/sr)
c	=	velocity of light, equal to 2.997925x10^{10} cm/s
e	=	electron charge, equal to 4.80298x10^{-10} cm$^{3/2}$g$^{1/2}$/s
f_{ij}	=	oscillator strength for the atomic line transition with a lower level i and an upper level j
g_i	=	degeneracy for an atomic level i
h	=	Planck's constant, equal to 6.6256x10^{-27} erg-s
I_λ	=	wavelength dependent intensity (erg/cm^3/sr/s)
j_{line}	=	wavelength-integrated emission coefficient over a single atomic line or multiplet (erg/cm^3/sr/s)
j_λ	=	wavelength dependent emission coefficient (erg/cm^4/sr/s)
J_c	=	wavelength-integrated normalized intensity for a given wavelength range (erg/cm^3/sr/s), which is often presented in this paper multiplied by 100, as indicated by *100
J_{line}	=	wavelength-integrated normalized intensity for a single atomic line or multiplet (erg/cm^3/sr/s)
J_{other}	=	normalized intensity resulting from atomic continuum, molecular bands, and weak atomic lines
J_λ	=	wavelength dependent intensity divided by the path length, or normalized intensity (erg/cm^4/sr/s)
N_a	=	number density of an atom a (particles/cm^3)
N_e	=	electron number density (particles/cm^3)
N_j	=	number density of an electronic atomic level j (particles/cm^3)
q_λ	=	wavelength dependent radiative flux directed towards the vehicle wall (W/cm^2/μ)
T_{ve}	=	vibrational-electronic-electron temperature (K)
T_e	=	electron temperature (K), assumed equal to T_{ve}
T_{tr}	=	translational-rotational temperature (K)
z	=	distance along the shock-tube axis from the shock front (cm)

* Aerospace Engineer, Member AIAA

Δx = path length of the intensity, equal to the shock-tube diameter (10.16 cm)
Δz_S = distance traveled by the shock during the measurement, which is accounted for with spatial smearing
$\Delta\lambda_T$ = full width at half max of the triangular slit function (nm)
$\Delta\lambda_D$ = Doppler broadening full width at half max (nm)
$\Delta\lambda_S$ = Stark broadening full width at half max (nm)
$\Delta\lambda_V$ = Voigt full width at half max (nm)
κ_λ = wavelength-dependent absorption coefficient (cm^{-1})
λ = wavelength (nm)
λ_{CL} = wavelength of the center of an atomic line transition (nm)
Subscripts
λ = indicates a wavelength dependence
i = refers to the lower electronic level of an atomic line transition
j = refers to the upper electronic level of an atomic line transition
Superscripts
a = indicates that spatial smearing and the finite slit width have not been accounted for.
b = indicates that the finite slit width has been accounted for.
line = indicates the value for a single atomic line.
Abbreviations
VUV = vacuum ultraviolet; refers to the spectral region below 200 nm

I. Introduction

The prediction of the shock-layer radiative heating to an entry vehicle at lunar-return conditions has received renewed interest due to NASA's plans for a return to lunar exploration. The prediction of the returning spacecraft's aerothermal environment during entry into Earth's atmosphere requires, among other things, the accurate modeling of the radiative heat flux resulting from the surrounding high-temperature shock-layer gas. Models developed for this purpose[1,2,3,4,5] have received limited experimental validation because of the scarcity of relevant experimental data, which include air radiation measurements at temperatures ranging from 9,000 to 11,000 K and pressures ranging from 0.1 – 1.0 atm.

The most widely considered data for radiation model validation are from the Fire II flight experiment[6,7]. This experiment obtained stagnation-point radiometer measurements of the wavelength-integrated intensity above 200 nm and spectrometer measurements of the wavelength-dependent intensity between 300 and 600 nm. The drawback of these measurements, for the purpose of model validation, is that they do not provide the spatial variation of the radiative intensity through the shock-layer, and they do not provide the spectral variation of the intensity in the significant 700 – 1200 nm range (or the 0 – 200 nm range). The spatial variation of the intensity is desired because it allows the nonequilibrium radiation behavior to be studied in detail, which provides an excellent assessment of the complex nonequilibrium chemistry and radiation models required for its prediction. The spectral dependence in the 700 – 1200 nm range is desired because it allows the significant nitrogen and oxygen atomic lines in this range to be studied in detail. The lack of these capabilities prevents the Fire II data from providing sufficient radiation model validation. Although predictions with the radiometer data are useful, the spatial and spectral integrations required to predict the wavelength-integrated intensity absorbed by the radiometer allow for fortuitous cancellations of errors, and therefore an inconclusive model validation. The Apollo 4 radiometer measurements[8] have similar limitations, as well as the added complexity of ablation products being present in the shock-layer. In addition to these two flight experiments, there have been several laboratory measurements of the radiative intensity reaching the body of a model placed in a shock tube[9,10,11,12]. These have been reviewed and compared with the RAD/EQUIL code by Sutton[13], but they also lack the desired spatial and spectral dependence.

Shock-tube measurements of the intensity profile behind a moving shock provide the desired spatially dependent radiation measurement. These have been reported by Allen et al.[14], Sharma[15,16,17], Donohue et al.[18], Koreeda et al.[19], Morioka et al.[20], Fujita et al.[21], and Matsuda et al.[22]. With the exception of Allen et al., these studies do not provide spectrally resolved data in the important 700 – 1200 nm range. Although Allen et al. did measure this range, the resolution is so coarse that the measurements do not allow the atomic-line shapes or the wavelength-integrated intensity resulting from an individual spectral feature to be studied. The 300 – 500 nm range measured in all of these studies is dominated by the N_2^+(1-) and N_2(2+) molecular band systems, which contribute significantly less than the atomic lines in the 700 – 1300 nm range at lunar return conditions. To the author's knowledge, the recent measurements by Grinstead et al.[23] in the NASA Ames Electric Arc Shock Tube (EAST) provide the only available

700 – 1300 nm spectrally resolved intensity data at lunar-return conditions. In addition to good spectral resolution in this desired range, these measurements also have good spatial resolution and a relatively long test length, which means that the details of both the nonequilibrium and equilibrium post-shock regions are captured. Spatially and spectrally dependent measurements are also available from Grinstead et al. in the 200 – 700 nm range. Figure 1 presents the wavelength-dependent radiative flux, between 0 and 1400 nm, at the stagnation point of NASA's Crew Exploration Vehicle (CEV) at a velocity of 10.5 km/s and an altitude of 57 km. The green curve presents the cumulative flux (and has units of W/cm^2), which indicates the contribution of each spectral range to the wavelength-integrated flux (note that only ~ 45 W/cm^2 is present above 1400 nm). The wavelength range of the EAST measurements by Grinstead et al. and Sharma are shown along with the range of the Fire II spectrometer. While the Sharma and Fire measurements cover less than 14% of the total flux, the Grinstead et al. measurements cover 52% of the total flux.

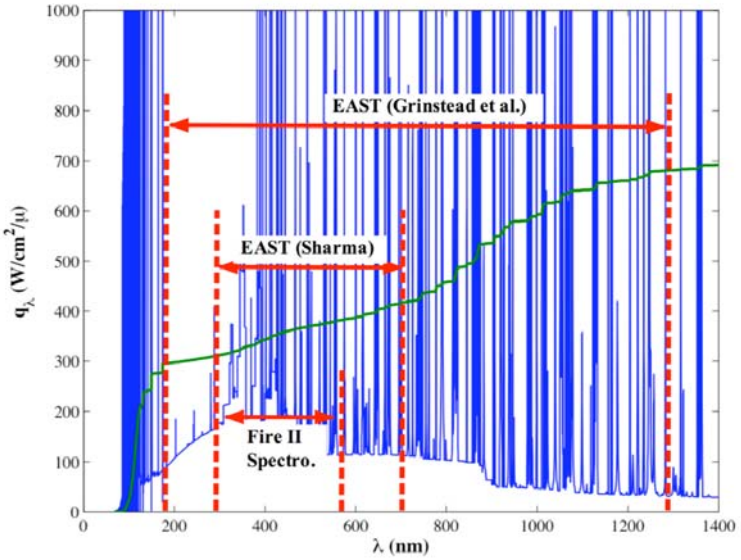

Figure 1. Radiative flux at the stagnation point of CEV at 10.5 km/s and 57 km (0.25 Torr), with a shock layer thickness of roughly 16 cm, a post-shock equilibrium temperature of 10,755 K, and a pressure of 0.47 atm.

The purpose of the present paper is to compare the High-temperature Air RAdiation (HARA) model developed by Johnston[1] with the measurements by Grinstead et al. for free-stream pressures of 0.1 and 0.3 Torr. Section II discusses the flowfield modeling and the spatial and spectral smearing required to convert the HARA predictions to the physical quantities measured by Grinstead et al.[23.] Section III presents the details of the HARA radiation model relevant to the data comparisons, which focuses on the atomic line contributions. The uncertainties in the atomic line broadening and oscillator strengths, obtained from published data, are presented for the most significant lines. Section IV presents the comparison of the HARA model with the 0.3 Torr measurements. These cases are in strong thermochemical equilibrium, which simplifies the theoretical modeling and causes the main uncertainties to be the line oscillator strengths and the line broadening widths. These uncertainties are addressed using the experimental measurements and published uncertainties for the line oscillator strengths and the line broadening widths as a guide. Section V presents the comparison of the HARA model with the 0.1 Torr measurements, which contain significant regions of thermochemical nonequilibrium and are nearly optically-thin. The main uncertainties for optically-thin nonequilibrium radiation are the electronic state populations of the radiating atomic species. The non-Boltzmann model used in HARA to calculate these populations has significantly larger uncertainties than the equilibrium radiation properties. Instead of the 10 to 30% uncertainty seen for line oscillator strengths and the line broadening widths, the nonequilibrium chemistry and non-Boltzmann rates have orders-of-magnitude uncertainties. These large uncertainties are due mainly to a lack of experimental measurements at the high-temperature conditions of interest in a peak-radiative heating shock-layer. The comparison between the HARA predictions and the measurements presented in Section V provides validation of the non-Boltzmann model applied in HARA. Section VI examines the equilibrium and nonequilibrium radiation from the 290 – 480 nm range, which is dominated by molecular band systems and atomic photoionization. The non-Boltzmann rates for the N_2^+(1-) and N_2(2+) band systems are adjusted to fit the nonequilibrium data. The 1020 – 1300 nm range is not considered in the present study, although these data are available. The radiation in this range is similar to that in the 700 – 1020 nm range, except weaker, so that validating the HARA model in the 700 – 1020 nm range indirectly validates the 1020 – 1300 nm range as well.

II. Simulating the Shock-Tube Radiation Measurements

Details of the shock-tube radiation measurements studied in this paper are reported by Grinstead et al.[23]. These measurements were performed in the NASA Ames EAST facility at initial pressures ranging from 0.1 to 1.0 Torr and shock velocities ranging from 9.1 to 11.1 km/s, with two different spectral ranges measured during each shot. The measured shock-velocity is reported to have an uncertainty of ±1.5%. Of the 46 reported shots, Table 1 lists the cases that are considered in the present comparison. These cases were chosen to include the spectral-regions that contribute the most to the radiative flux at lunar-return peak heating. For each spectral range chosen, both the 0.1 and 0.3 Torr cases are considered. The 0.1 Torr cases contain significant regions of nonequilibrium, which will be used to validate both the nonequilibrium flowfield and nonequilibrium radiation modeling. Also, these cases are nearly optically-thin, which will provide a useful model simplification. On the other hand, the 0.3 Torr cases are optically thick but have significant regions of equilibrium radiation.

Table 1. Conditions and measurement parameters for the EAST shock-tube cases considered in this study.

Case ID	λ-range (nm)	Shock Velocity (km/s)	Initial Pressure (Torr)	Test Length (cm)	$\Delta\lambda_T$ (nm)	Δz_S (cm)	Shot #
1	700 - 900	10.34	0.3	7.6	1.7	0.078	45
2	900 - 1020	9.880	0.3	7.8	2.0	0.97	46
3	700 - 900	9.165	0.1	2.6	1.7	0.46	7
4	900 - 1020	9.989	0.1	5.8	2.0	0.98	2
5	290 - 480	10.34	0.3	7.6	0.8	0.25	45
6	290 - 480	9.663	0.1	4.3	0.8	0.98	9

The radiative intensity emitted from the shock-tube was measured with varying degrees of spatial and spectral resolution, depending on the wavelength region being measured. The spectral resolution was mainly a function of the spectrograph exposure time, which smeared the spatial resolution by the distance the shock traveled in that time (Δz_S). This is illustrated in Figure 2, which shows the radiative intensity profile measured between the time t and t-Δt. The measured value is the average of the profiles collected in this period of time. The spectral resolution is defined by the spectrograph slit width ($\Delta\lambda_T$), meaning the measured intensity at a specified wavelength is actually the average value of the wavelength-dependent intensity multiplied by a triangular function (centered at the specified wavelength) with a full-width at half-height equal to the slit width. The methodology for simulating the slit width and spatial smearing in the predictions will be discussed in the following paragraphs.

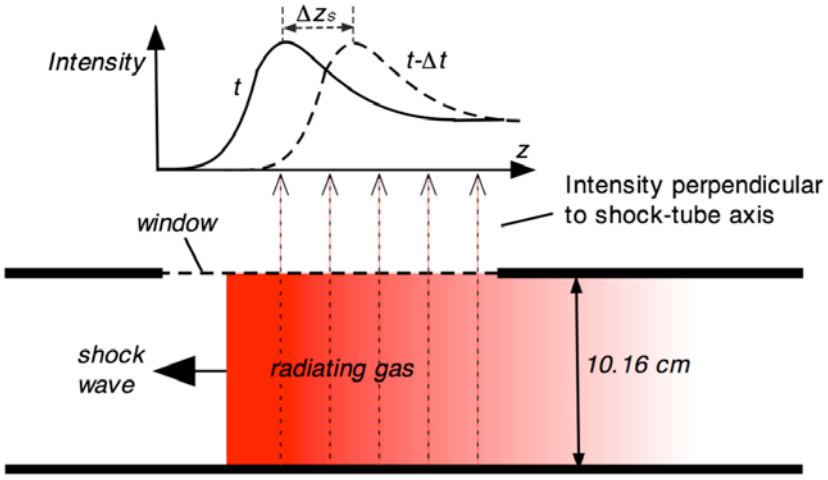

Figure 2. Schematic (not to scale) of the EAST shock-tube measurements simplified to the configuration modeled in the present analysis.

The shock-tube flowfield was simulated using the LAURA Navier-Stokes solver to predict the flow around a 5 m sphere at the specified shock-tube conditions. A two-temperature thermochemical nonequilibrium 11-species (N_2, N_2^+, O_2, O_2^+, NO, NO^+, N, N^+, O, O^+, and e^-) air model was applied in these computations[24,25,26]. The resulting LAURA flowfields for Cases 1 – 4 are presented in Figures 3 and 4. Only the number densities relevant to the radiation calculations are presented in these figures. Note that the 5 m sphere provides a stagnation-line shock-layer thickness of roughly 20 cm, which leaves (at least) the first 6 cm behind the shock free of boundary layer and

pressure gradient effects. This ~6 cm region behind the shock provides a one-dimensional model of the shock-tube flowfield, which is assumed constant in the radial direction. The shock-tube boundary layer was not treated, since it has been shown[7] to have a negligible influence on the spectral ranges presently considered. Also, note that radiative cooling was not included in the flowfield computations because of the significant complications required for its treatment. These complications include the prediction of radiation from the downstream contaminated regions, which are unknown, and a radiation transport calculation that accounts for the reflection of intensity rays from the shock-tube walls, which means the tangent slab approximation is not valid. Fortunately, not accounting for radiative cooling should have a negligible influence on the present study for several reasons. First, most of this study will examine regions of the shock-layer less than 4 cm from the shock front, which means the gas has had little time to emit energy. Analogous to this is the statement that a thinner shock-layer is influenced less from radiative cooling than a thicker shock-layer at the same conditions. Second, the reflection of intensity rays off of the shock-tube walls prevents much of the emitted energy from escaping the shock-layer. This means the cooling should be less than that predicted for a tangent-slab, which does not account for this. Finally and most convincingly, if radiative cooling did influence the present measurements, a gradual decrease in the intensity (a well-known characteristic of the radiative cooling of external shock-layers) should be seen for the highly radiating 0.3 Torr measurements, which it is not (as will be shown).

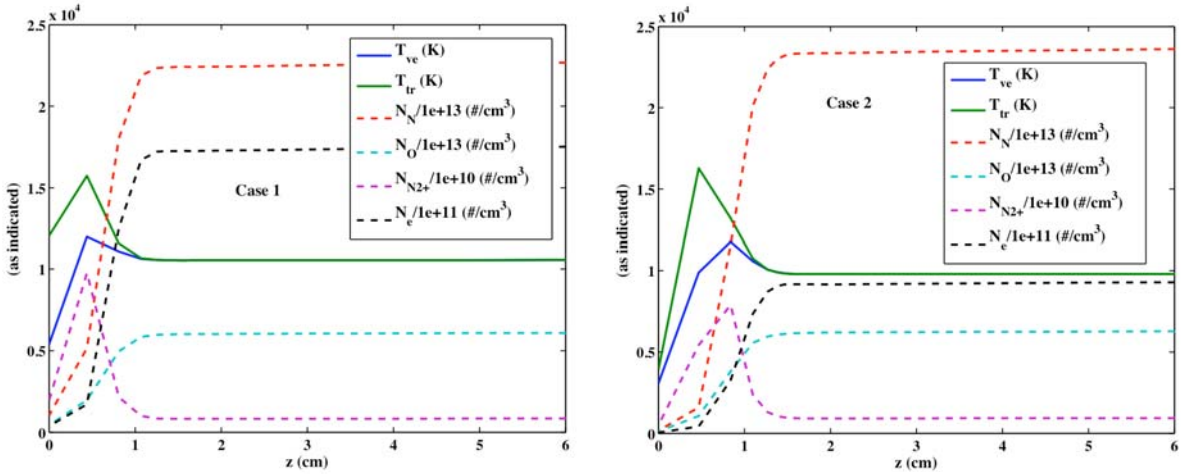

Figure 3. Temperatures and relevant number densities predicted by LAURA for Cases 1 and 2, both at 0.3 Torr.

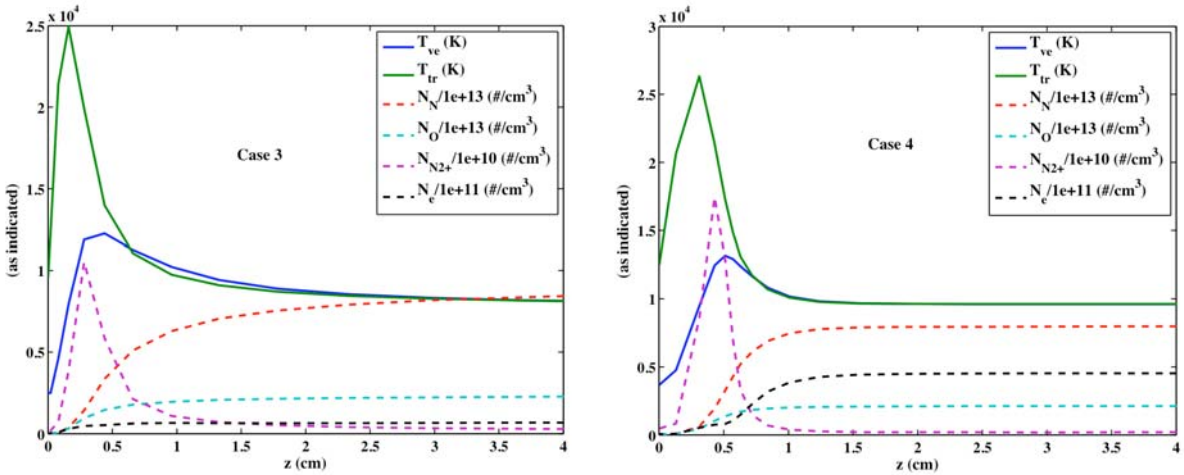

Figure 4. Temperatures and relevant number densities predicted by LAURA for Cases 3 and 4, both at 0.1 Torr.

From the temperatures and number densities of the computed one-dimensional flowfield, the normalized radiative intensity (J_λ), which is equal to the intensity divided by the length of the emitting gas, was obtained at each z-location using the wavelength-dependent emission (j_λ) and absorption (κ_λ) coefficients predicted by HARA (the

details of which will be presented in the next section), and the radiative transfer equation for the intensity resulting from a constant property line-of-sight, which is written as

$$J_\lambda^a = \frac{1}{\Delta x}\frac{j_\lambda}{\kappa_\lambda}\left[1-\exp\left(-\kappa_\lambda \Delta x\right)\right] \tag{1}$$

where Δx is the diameter of the shock-tube and is equal to 10.16 cm. The superscript a indicates that the spatial smearing and finite slit-width have not been accounted for. The predicted intensity accounting for the slit-width (J_λ^b) is obtained from the following convolution

$$J_\lambda^b = \frac{1}{\Delta\lambda_T}\int_{\lambda-\Delta\lambda_T}^{\lambda+\Delta\lambda_T} J_{\tilde{\lambda}}^a C\left(\tilde{\lambda},\lambda\right)d\tilde{\lambda}, \qquad C\left(\tilde{\lambda},\lambda\right) = 1-\frac{\left|\lambda-\tilde{\lambda}\right|}{\Delta\lambda_T} \tag{2}$$

where $\Delta\lambda_T$ is the full-width at half-height of the triangular instrument function C. A final convolution is performed to account for the spatial smearing due to the spectrograph exposure time:

$$J_\lambda(z) = \frac{1}{\Delta z_S}\int_z^{z+\Delta z_S} J_\lambda^b(\tilde{z})d\tilde{z} \tag{3}$$

where Δz_S is equal to the shock velocity multiplied by the exposure time. The $\Delta\lambda_T$ and Δz_S values required for Eqs. (2) and (3) are provided by Grinstead et al. and are listed in Table 1. The J_λ values resulting from Eq. (3) will be the subject of the comparisons with the EAST data throughout this paper, unless indicated otherwise. Note that the influence of the spatial smearing is only to smooth out the nonequilibrium post-shock zone; it does not influence the equilibrium region. An example of this is shown in Figure 5, which presents the integrated intensity over a specified wavelength range (700 – 760 nm) with and without spatial smearing. Also worth noting is that the slit-widths are small enough in the present study that they do not noticeably alter the wavelength-integrated intensity if the size of the wavelength region being integrated is greater than $\Delta\lambda_T$. This will be useful when comparing the integrated intensity from a group or a single atomic line.

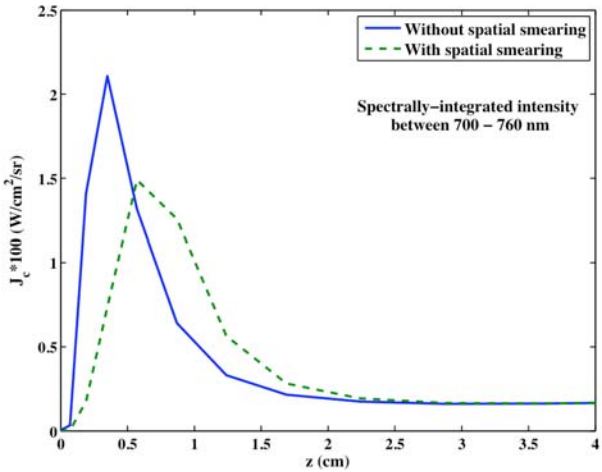

Figure 5. The influence of spatial smearing for Case 3.

III. Radiation Modeling

The High-temperature Air RAdiation (HARA) code developed at NASA Langley Research Center was applied in the present study. This code provides an efficient and detailed method for calculating shock-layer radiation. Complete details of the non-Boltzmann, atomic line, atomic photoionization, and molecular band models applied in HARA are presented in Ref. 1. The modeling details relevant to the present comparison with the EAST data are reviewed here.

The most significant contributor to the radiation at the conditions and spectral ranges of interest in the present study are atomic lines. The wavelength-dependent emission coefficient resulting from a single atomic line transition, from the lower level i to the upper j, is written as[27]

$$j_{\lambda,ij}^{line} = N_j \frac{2\pi h e^2}{mc^3}\left(\frac{c}{\lambda_{CL}}\right)^3 \frac{g_i}{g_j} f_{ij} b_\lambda \qquad \left(\frac{erg}{cm^4\cdot sr\cdot s}\right) \tag{4}$$

where N_j is the number density of the upper level, f_{ij} is the oscillator strength, and b_λ is the wavelength dependent shape function. Similarly, the absorption coefficient is written as[27]

$$\kappa_{\lambda,ij}^{line} = N_i \frac{\pi e^2 \lambda_{CL}^2}{mc^2} f_{ij} b_\lambda \qquad (cm^{-1}) \tag{5}$$

which is dependent on the lower level number density N_i. The wavelength dependent shape function (b_λ) is defined by the Lorentzian ($\Delta\lambda_L$) and Gaussian ($\Delta\lambda_G$) full-widths at half-max (FWHM). For the presently studied lunar-return conditions, which have temperatures on the order of 10,000 K and relatively high pressures and electron number densities, $\Delta\lambda_L$ is essentially equal to the Stark broadening width ($\Delta\lambda_S$), and $\Delta\lambda_G$ is essentially equal to the Doppler broadening width ($\Delta\lambda_D$). The Stark broadening width may be written as[28]

$$\Delta\lambda_S = \Delta\lambda_{S,0}\left(\frac{T_e}{10{,}000}\right)^n \left(\frac{N_e}{1\times10^{16} cm^{-3}}\right) \tag{6}$$

where $\Delta\lambda_{S,0}$ is the theoretically or experimentally determined Stark FWHM at temperature of 10,000 K and an electron number density (N_e) of $1x10^{16}$ #/cm^3, and n represents the assumed temperature dependence, which is assumed equal to 1/3 in the present study. The Doppler FWHM is written as[28]

$$\Delta\lambda_D = 2\frac{\lambda_{CL}}{c}\left(\frac{2kT_e \ln(2)}{m_s}\right)^{1/2} \tag{7}$$

where m_s is the mass (g/particle) of the radiating species.

The data required for implementing Eqs. (4 – 7) for the most significant lines in the 700 – 1020 nm range are listed in Table 2. This table actually lists the multiplet averaged value, with the number of lines associated with each multiplet listed in the *#lines* column. Although HARA treats each individual line of a multiplet separately, it is convenient to refer to multiplets throughout the discussion. The *i* and *j* columns refer to the upper and lower electronic states of the transition, as defined in Ref. 1. The f_{ij} values and uncertainties (f_{ij} *%unc.*) are taken from Wiese et al.[29] while the Stark broadening coefficients and uncertainties ($\Delta\lambda_{S,0}$*%unc.*) are taken from the source listed in the last column.

Table 2. A list of multiplets that contribute significantly to the present cases.

ID#	Species	Wiese ID[a]	# Lines	$\lambda_{CL,mult}$ *(nm)*[b]	*i* [c]	*j*	f_{ij}	f_{ij} *%unc.*	$\Delta\lambda_{S,0}$ *(nm)*	$\Delta\lambda_{S,0}$ *%unc.*	$\Delta\lambda_{S,0}$ *ref.*
1	N	48	3	745.42	4	10	1.05e-1	3	8.55e-3	30	30
2	*O*	*56*	*3*	*777.55*	*4*	*6*	*1.00e+0*	*3*	*6.30e-3*	*50*	*31*
3	N	47	7	821.41	4	9	3.14e-1	3	8.90e-3	30	30
4	*O*	*60*	*3*	*844.88*	*5*	*7*	*1.03e+0*	*10*	*1.28e-2*	*50*	*31*
5	N	52	4	861.98	5	12	3.51e-1	10	1.56e-2	30	30
6	N	46	8	869.40	4	8	4.66e-1	10	1.18e-2	30	30
7	N	65	2	905.24	7	16	1.10e+0	10	4.03e-2	30	30
8	N	127	3	905.01	13	28	4.80e-1	10	3.10e-2	30	30
9	N	126	4	919.82	13	28	3.31e-1	25	2.54e-1	100	1
10	*O*	*64*	*9*	*926.64*	*6*	*10*	*9.55e-1*	*3*	*4.44e-2*	*50*	*31*
11	N	51	3	939.79	5	11	5.81e-1	10	1.43e-2	50	31
12	N	72	10	983.33	8	20	1.36e-1	10	4.50e-2	50	31
13	N	70	4	998.70	8	18	2.57e-2	25	6.22e-2	100	1
14	N	71	8	999.10	8	19	3.90e-1	25	6.22e-2	100	1
15	N	69	9	1011.7	8	17	8.05e-1	10	8.21e-2	50	30
16	*O*	*59*	*2*	*1016.8*	*5*	*6*	*1.24e-5*	*25*	*1.22e-2*	*50*	*31*

[a] Multiplet number assigned by Wiese et al.[29]
[b] multiplet averaged wavelengths listed for a vacuum
[c] *i* and *j* are defined in Tables 3.1 and 3.2 of Ref. 1

If it is assumed that the lines do not overlap and that other radiation mechanisms are negligible, the (normalized) intensity from a single line may be written from Eq. (1) as

$$J_{\lambda,ij}^a = \frac{1}{\Delta x}\frac{j_{\lambda,ij}^{line}}{\kappa_{\lambda,ij}^{line}}\left[1-\exp\left(-\kappa_{\lambda,ij}^{line}\Delta x\right)\right] \tag{8}$$

The HARA code does *not* treat each line separately (meaning it accounts for overlapping lines) and it *does* account for other radiation mechanisms (such as atomic photoionization, molecular bands, and the influence of induced emission on κ_λ), but these will have minimal influence on the present results, so that Eq. (8) provides a convenient means for understanding the transport of each atomic line.

For the 0.1 Torr cases presented in Section V, the negative value in the exponential of Eq. (8) is much less than 1 at the center of most lines. As a result, the exponential may be expanded in Taylor series, which simplifies Eq. (8) to

$$J^{a}_{\lambda,ij} = j^{line}_{\lambda,ij} \tag{9}$$

This is the optically-thin approximation, which is useful because it allows the wavelength-integrated intensity of a single line to be written from Eq. (4) as

$$J^{a}_{ij} \approx J^{b}_{ij} = N_j \frac{2\pi hc^2}{mc^3}\left(\frac{c}{\lambda_{CL}}\right)^3 \frac{g_i}{g_j} f_{ij} \quad \left(\frac{erg}{cm^3 \cdot sr \cdot s}\right) \tag{10}$$

Since the f_{ij} values are relatively well known for each line (see Table 2), this equation provides a relationship between J_{ij}, which may be inferred from the EAST measurements, and the number density of the radiating level N_j (the conversion from J^{b}_{ij} calculated in Eq. (10) to J_{ij}, which is consistent with the measured quantity, is achieved using Eq. (3)). Thus, the N_j values inferred from the nearly optically-thin 0.1 Torr EAST measurements may be compared with those predicted by the HARA non-Boltzmann model, which provides a valuable set of data for validating the non-Boltzmann model. These data may also be used to indirectly validate the nonequilibrium LAURA flowfield model, whose predicted temperatures and number densities drive the non-Boltzmann model.

For the 0.3 Torr cases presented in Section IV, the optically-thin approximation is not valid, and the connection between the N_j and J_{ij} provided by Eq. (10) is not applicable. Not only does the higher pressure increase the optical-thickness, but it also decreases the size of the nonequilibrium region of the shock layer. Therefore most of the shock-layer is in thermochemical *equilibrium*, which simplifies the prediction of N_j to simply that of a Boltzmann distribution. As a result, Eq. (8) simplifies to

$$J^{a}_{\lambda,ij} = \frac{1}{\Delta x} B_\lambda \left[1 - \exp\left(-\kappa^{line}_{\lambda,ij} \Delta x\right)\right] \tag{11}$$

where B_λ is the well-known Planck function. The main complication in this case is the prediction of line-shape function b_λ, which depends primarily on the Stark and Doppler line-widths discussed previously[32]. The comparison between the measured line-shapes and the predicted line shapes is not possible because the finite slit-width (accounted for in Eq. (2)) widens and distorts each line considerably. This slit-width convolution does not noticeably change the integrated intensity over a given line or set of lines. Therefore, comparisons between the measured and predicted wavelength integrated intensity provide an indirect method for validating the Stark and Doppler line-width models.

A smeared rotational band (SRB) approach is applied for modeling the molecular band systems[33]. Of interest in the present study are the N_2^+(1-), N_2(2+), and CN violet band systems, which contribute to the 290 – 480 nm spectral range considered in Section VI. The data required for modeling these bands are taken from Laux[34]. For 0.1 and 0.3 Torr conditions, these band systems are optically-thin. The SRB model is therefore accurate at predicting the wavelength-integrated intensity to within a few percent[35].

Before the comparisons between the predictions and measurements are presented, two significant caveats of this analysis must be mentioned. The first is that the influence of the ±1.5% uncertainty on the measured shock velocity was considered for each case. The sensitivities of the radiation to these plus and minus velocity uncertainties are of roughly equal magnitude. Therefore, only the velocity change, either plus or minus, that improves the comparison with the measurements will be presented, although the influence of the opposite change may be assumed to have similar magnitude, but opposite sign. The second caveat of this analysis, which applies only to Cases 1 and 5, is that a constant value (0.8 and 1.5 W/cm^3/sr/μ for Cases 1 and 5, respectively) was subtracted from the measurements. This was done to force the predictions and measurements to agree in the atomic continuum dominated regions of the spectrum, which do not contain atomic lines or molecular band systems, but are susceptible to calibration errors and radiation from contamination species. Forcing the continuum to agree allows these issues to be avoided and clarifies the atomic line and molecular band contributions.

IV. Comparison with the 0.3 Torr Measurements

A significant fraction of the radiative heating at typical peak-heating lunar-return conditions is emitted from shock-layer regions in thermochemical *equilibrium*. According to flowfield predictions shown in Figure 2, the 0.3 Torr EAST cases are in thermochemical equilibrium throughout most of the usable test time. Thus, they provide a valuable means for validating the present radiation model in the important equilibrium regime. Comparisons between experiment and predictions in this regime are also valuable because the problems of nonequilibrium chemistry and non-Boltzmann state-populations do not complicate the theoretical modeling. As a result, the main uncertainties in the radiation prediction are the line oscillator strengths and the line broadening widths. Addressing these uncertainties for the atomic-lines in the 700 – 1020 nm range, using the experimental measurements as a guide, is the subject of this section.

A comparison between the measured and predicted intensity spectrum (J_λ) at 3.2 cm behind the shock is shown in Figure 6 for the 10.34 km/s case at 0.3 Torr (Case 1 in Table 1). The measured wavelength range for this case is 700 – 900 nm, with the dominant spectral features being the first 6 atomic line multiplets listed in Table 2. The significance of these various spectral features is indicated in this figure by the cumulative wavelength-integrated (J_c) curve, which has been multiplied by 100 for scaling purposes. Note that a constant value of 0.8 W/cm^3/sr/μ was subtracted from the measurements for this case to force the continuum radiation to agree, as mentioned previously. This subtracted value, which result is a total J_cx100 of 14.4 W/cm^3/sr, is interpreted as an artifact of calibration or an untreated radiation mechanism from contamination species. The J_c predictions at shock-velocities 1.5% below the specified value are shown in Figure 6 to indicate the sensitivity to the reported uncertainty in the measured shock-velocity. The agreement between the measured and predicted J_c values is within 10% throughout this wavelength range. Similar agreement is seen in Figures 7 and 8, which show J_c values from three selected wavelength ranges (which are actually ΔJ_c values, meaning they are contribution from only the specified wavelength range) as a function of the post-shock distance (z). The influence of the 1.5% shock-velocity uncertainty is shown in these figures along with the prediction obtained by assuming a Boltzmann distribution of electronic states. The Boltzmann and non-Boltzmann predictions are seen to converge in the regions of thermochemical nonequilibrium, as they should.

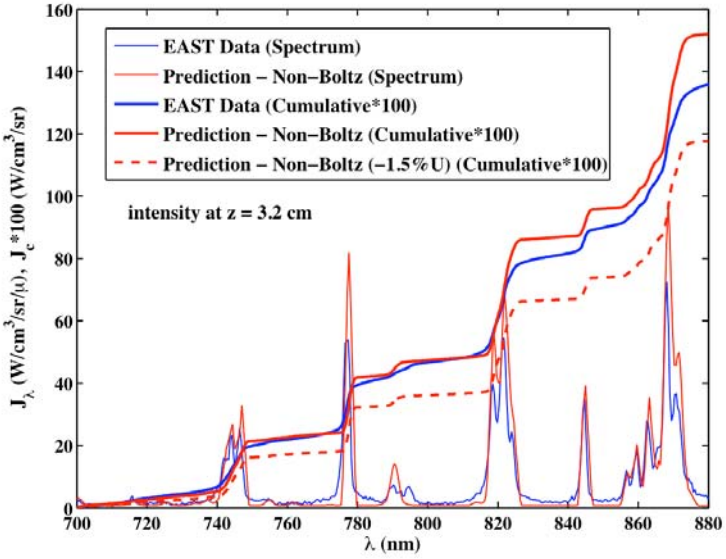

Figure 6. Comparison of the predicted and measured spectrum at z = 3.2 cm for Case 1.

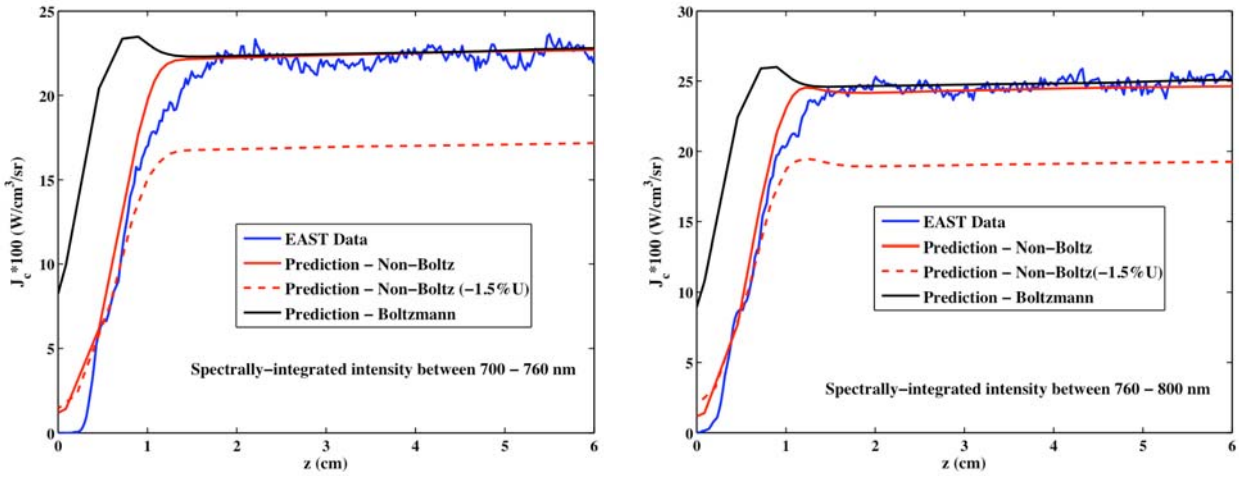

Figure 7. Spatial variation of the normalized intensity integrated over the 700-760 and 760-800 nm wavelength ranges for Case 1.

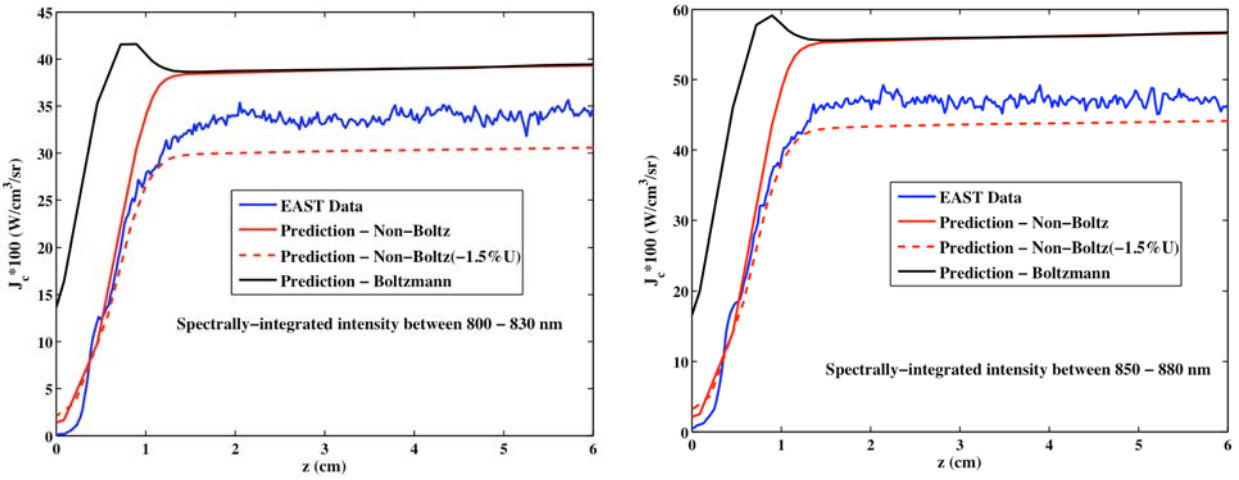

Figure 8. Spatial variation of the normalized intensity integrated over the 800-830 and 850-880 nm wavelength ranges for Case 1.

The measured and predicted values for the 900 – 1020 nm spectral range are compared in Figures 9 – 11 for the 9.88 km/s 0.3 Torr case (Case 2 in Table 1). The dominant spectral features in this wavelength range are the atomic lines associated with multiplets 7 – 16 listed in Table 2. A slight over-prediction of the measurements is seen for most of the spectrum in Figure 9, which is taken in the equilibrium region of the flow (z = 3.5 cm). Note that the multiplets around 920 nm and 1000 nm are significantly over-predicted. The 920 nm multiplet is listed as multiplet 9 in Table 2, and the 1000 nm multiplet is a combination of multiplets 13 and 14. These multiplets have the highest uncertainties for both f_{ij} and $\Delta\lambda_{S,0}$, with each being 25% and 100%, respectively. The influence of these uncertainties, along with the general over-prediction seen throughout this spectral range, will be discussed further in the following paragraphs. A distinct difference between the profiles for Case 2 (Figures 10 and 11) and Case 1 (Figures 7 and 8) is the size of the nonequilibrium region, which is identified as the region where the Boltzmann and non-Boltzmann predictions are not coincident. This difference is a result of the lower shock velocity for Case 2. The profiles predicted by the non-Boltzmann model compare well with the data in the nonequilibrium regions, especially when compared with the Boltzmann results. The gradual rise in the measurements seen beyond 4 cm in Figures 10 and 11 is possibly due to the onset of driver gas contamination[23]. Note that this gradual increase is opposite in sign of the gradual decrease expected if radiative cooling was significant.

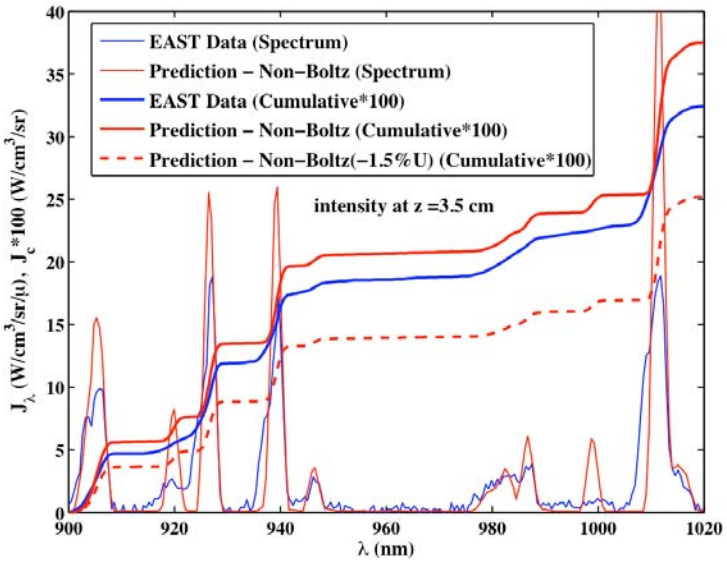

Figure 9. Comparison of the predicted and measured spectrum at z = 3.5 cm for Case 2.

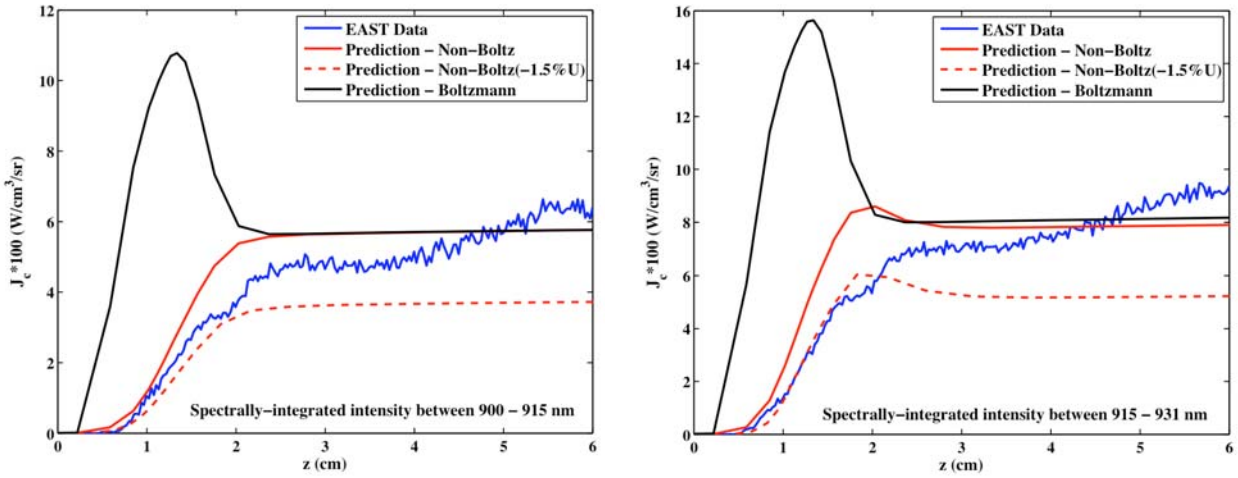

Figure 10. Spatial variation of the normalized intensity integrated over the 900-915 and 915-931 nm wavelength ranges for Case 2.

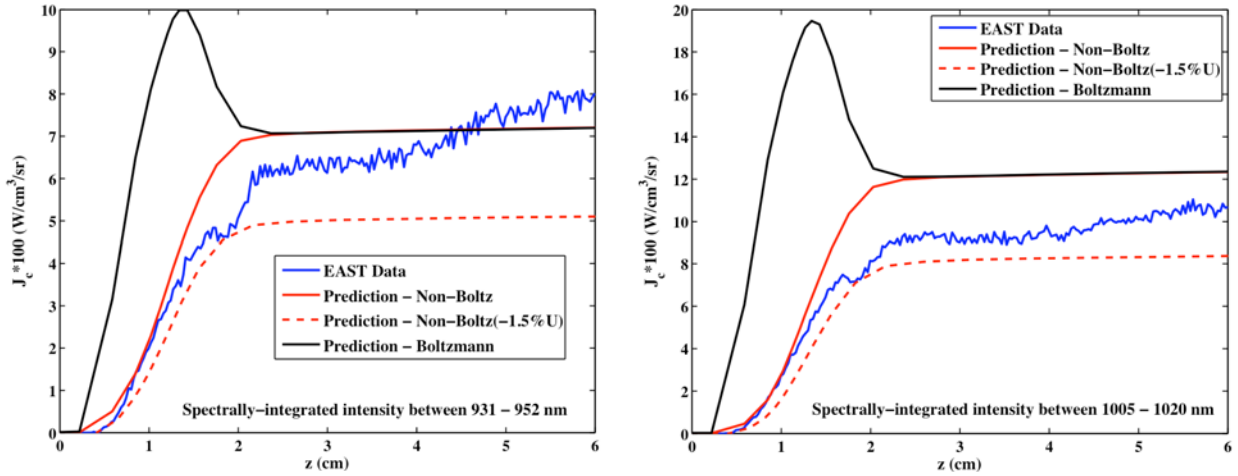

Figure 11. Spatial variation of the normalized intensity integrated over the 931-952 and 1005-1020 nm wavelength ranges for Case 2.

Further insight into the present comparison between the measured and predicted equilibrium radiation is gained by examining the predicted contributors to the spectral features in Figures 6 and 9. Tables 3 and 4 present a detailed breakdown of these spectral features by dividing the 700 – 1020 nm spectral range into 11 sections, with the wavelength boundaries specified in the first column. Each of these sections contains either one or two of the strong multiplets listed in Table 2. The details of the intensity contributions from each these multiplets are presented in columns 2 – 7, which are discussed in the following paragraphs.

The listed $\Delta\lambda_S$ and $\Delta\lambda_D$ values represent characteristic values for the multiplet, which are actually slightly different for each line in the multiplet. These are shown for each multiplet to indicate the width of the lines in the multiplet ($\Delta\lambda_V$), where $\Delta\lambda_V \sim \Delta\lambda_S + \Delta\lambda_D$ for the present cases. Also, the size of $\Delta\lambda_S$ relative to $\Delta\lambda_D$ will be shown to have an influence on the sensitivity of the predicted intensity to $\Delta\lambda_S$. This sensitivity to $\Delta\lambda_S$ is of interest because of the significant $\Delta\lambda_S$ uncertainties, which are listed in Table 2 for each multiplet. It is seen for the present cases that $\Delta\lambda_S$ and $\Delta\lambda_D$ are of roughly equal magnitude, so sensitivity to $\Delta\lambda_S$ is expected, although its magnitude is also dependent on the optical thickness of the lines in the multiplet.

The listed j_{line} and J_{line} values are the emission coefficient and normalized intensity, respectively, resulting from only the specified multiplet. These two values are presented to indicate the optical thickness of the lines in the multiplet, where the larger the reduction of J_{line} relative to j_{line}, the larger the optical thickness. It is seen in the present cases that most of the 700 – 880 nm multiplets are optically-thick ($J_{line}/ j_{line} < 0.5$), while only a few are in the 900 – 1020 nm range. The larger the optical-thickness, the more the intensity is sensitive to $\Delta\lambda_S$. This is shown in the $\%\Delta J_{total}(\Delta\lambda_S)$ column, which lists the percent decrease in the total intensity from the specified wavelength range due to a 30% decrease in $\Delta\lambda_S$ (the total intensity (J_{total}) includes J_{other} in addition to J_{line}, which will be

discussed). A decrease of less than 10% is seen for each case, with the largest being the optically-thick multiplets in the 800 – 830 nm and 931 – 952 nm ranges, for which cases $J_{line}/\ j_{line} \sim 0.4$. The reason why the wavelength-integrated intensity for an optically thick line is strongly dependent upon $\Delta\lambda_S$, while an optically thin line is not, is that the height of an optically-thick line is blackbody limited, so that the integrated intensity is governed only by the width of the line, which is not influenced by the optical thickness.

The wavelength-integrated intensity is also sensitive to f_{ij}. The f_{ij} uncertainties are listed in Table 2 for each multiplet and are on the order of 10%. The $\%\Delta J_{total}(f_{ij})$ column lists the percent decrease in the total intensity from the specified wavelength range due to a 10% decrease in f_{ij}. It is seen that the nearly optically-thin cases decrease almost proportionally with f_{ij}, while the optically-thick cases are influenced less. The blackbody limiting of the optically-thick lines causes their sensitivity to f_{ij} to be less than for an optically-thin line. The $\Delta\lambda_S$ and f_{ij} sensitivities examined here for the wavelength-integrated intensity, when combined with their uncertainties listed in Table 2, provide legitimate rational for disagreements between predictions and the EAST measurements, as will be discussed. Although only decreases in $\Delta\lambda_S$ and f_{ij} were presented, the results obtained by increasing these values are of similar magnitude and opposite sign.

The J_{other} column in Tables 3 and 4 lists the normalized intensity contributions from mechanisms other than the identified multiplets. These values are a result mostly of atomic-photoionization and relatively weak atomic lines. The sum of J_{other} and the J_{line} value(s) in the given wavelength range results in the total predicted normalized intensity in that range, which is listed in the J_{total} column. The corresponding EAST measurement of this value is listed in the J_{EAST} column, and the percent difference between J_{total} and J_{EAST} is listed in the *%diff* column. To account for the noise in the data, the J_{EAST} values presented in these tables are actually averaged values over 0.4 cm around the specified *z*-location. Recall that for the Case 1 results shown in Table 3, measurements were only available for the 700 – 880 nm range, while for Case 2 in Table 4, they were only available for the 900 – 1020 range. The total percent difference between the predictions and measurements, or from the sensitivities, are listed below each measurement range. This value is somewhat misleading because the negative and positive values cancel each other for some cases.

Table 3. Breakdown of measurements and predictions for Case 1 at *z* = 3.2 cm[a].

λ-range (nm)	Mult. ID#	λ_{CL} (nm)	$\Delta\lambda_S$ (nm)	$\Delta\lambda_D$ (nm)	j_{line} x100	J_{line} x100	J_{other} x100	J_{total} x100	J_{EAST} x100	% diff	$\%\Delta J_{total}$ $(\Delta\lambda_S)$[b]	$\%\Delta J_{total}$ (f_{ij})[c]	$\%\Delta J_{total}$ (U)[d]
700-760	1	745.4	1.5e-2	1.4e-2	27.3	14.6	8.11	22.8	21.8	-4.4	-6.8	-3.9	-25
760-800	2	777.5	1.1e-2	1.4e-2	50.1	16.5	7.88	24.4	24.2	-0.8	-8.9	-3.4	-22
800-830	3	821.4	1.5e-2	1.6e-2	72.6	31.8	7.10	38.8	33.5	-13	-9.6	-4.7	-22
830-850	4	844.8	1.8e-2	1.5e-2	18.4	7.82	1.64	9.46	10.0	5.7	-9.0	-5.5	-20
850-880	5	861.9	2.6e-2	1.7e-2	25.7	15.2	3.94	55.9	46.7	-17	-11	-5.5	-22
	6	869.4	1.8e-2	1.7e-2	99.6	36.8							
								Total	=	-10	-9.5	-4.7	-22
900-915	7	*905.2*	7.1e-2	1.8e-2	9.01	7.63	0.73	15.4	-	-	-5.5	-8.1	-26
	8	*905.0*	5.5e-2	1.8e-2	8.64	7.10							
915-931	9	*919.8*	4.5e-1	1.8e-2	5.45	5.22	1.21	20.2	-	-	-2.9	-8.6	-25
	10	*926.6*	7.9e-2	1.7e-2	19.2	13.8							
931-952	11	*939.7*	2.5e-2	1.8e-2	37.4	14.7	1.63	16.3	-	-	-12	-5.0	-22
952-995	12	*983.3*	7.9e-2	1.9e-2	8.24	7.45	2.00	9.45	-	-	-1.9	-7.4	-26
995-1005	13	*998.7*	1.1e-1	1.9e-2	1.52	1.44	0.43	4.00	-	-	-2.0	-8.4	-28
	14	*999.1*	1.1e-1	1.9e-2	2.32	2.13							
1005-1020	15	*1011*	7.8e-2	1.9e-2	46.9	28.7	1.01	29.7	-	-	-9.5	-7.0	-23
								Total	=	-	-6.8	-7.3	-24

[a] $T_{tr} = T_{ve} = 10{,}550$ K, $N_N = 2.25\text{e+}17$, $N_O = 6.05\text{e+}16$, $N_e = 1.74\text{e+}16$ particles/cm^3

[b] Percent change of J_{total} due to a 30% decrease in all $\Delta\lambda_S$ values.

[c] Percent change of J_{total} due to a 10% decrease in all f_{ij} values.

[d] Percent change of J_{total} due to a 1.5% decrease in the shock velocity.

Table 4. Breakdown of measurements and predictions for Case 2 at z = 3.5 cm[a].

λ-range (nm)	Mult. ID#	λ_{CL} (nm)	$\Delta\lambda_S$ (nm)	$\Delta\lambda_D$ (nm)	j_{line} x100	J_{line} x100	J_{other} x100	J_{total} x100	J_{EAST} x100	% diff	$\%\Delta J_{total}$ ($\Delta\lambda_S$)	$\%\Delta J_{total}$ (f_{ij})	$\%\Delta J_{total}$ (U)
700-760	1	745.4	7.8e-3	1.4e-2	10.7	6.51	2.56	9.07	-	-	-4.9	-4.7	-32
760-800	2	777.5	5.8e-3	1.4e-2	21.0	8.33	2.56	10.9	-	-	-6.9	-3.7	-28
800-830	3	821.4	8.3e-3	1.6e-2	28.9	14.5	2.23	16.8	-	-	-7.0	-5.1	-28
830-850	4	844.8	9.4e-3	1.5e-2	7.55	3.95	0.55	4.49	-	-	-6.3	-5.9	-25
850-880	5	861.9	1.4e-2	1.6e-2	9.98	6.45	1.16	24.3	-	-	-8.6	-5.7	-28
	6	869.4	8.8e-3	1.7e-2	39.9	16.7							
								Total	=	-	-7.2	-5.1	-28
900-915	7	*905.2*	3.7e-2	1.7e-2	3.27	2.87	0.17	5.57	4.47	-20	-4.0	-8.6	-34
	8	*905.0*	2.8e-2	1.7e-2	2.93	2.53							
915-931	9	*919.8*	2.3e-1	1.7e-2	1.91	1.85	0.28	7.79	7.09	-8.9	-2.7	-8.9	-33
	10	*926.6*	4.1e-2	1.6e-2	7.21	5.65							
931-952	11	*939.7*	1.3e-2	1.8e-2	14.7	6.47	0.46	6.92	6.36	-8.1	-9.9	-5.2	-28
952-995	12	*983.3*	4.1e-2	1.9e-2	2.97	2.79	0.55	3.35	3.78	13	-1.6	-7.9	-36
995-1005	13	*998.7*	5.5e-2	1.9e-2	0.55	0.53	0.10	1.42	0.60	-58	-1.8	-8.8	-35
	14	*999.1*	5.5e-2	1.9e-2	0.84	0.79							
1005-1020	15	*1011*	4.0e-2	1.9e-2	16.9	12.1	0.20	12.3	9.17	-25	-8.2	-7.4	-33
								Total	=	-16	-5.9	-7.6	-33

[a] $T_{tr} = T_{ve}$ = 9,797 K, N_N = 2.35e+17, N_O = 6.24e+16, N_e = 9.22e+15 particles/cm^3

V. Comparison with the 0.1 Torr Measurements

The prediction of nonequilibrium radiation is dependent upon the modeling of the nonequilibrium chemistry and the non-Boltzmann population of the radiating states, in addition to the oscillator strengths and line-widths required for equilibrium radiation predictions. The nonequilibrium chemistry and non-Boltzmann models, which are assumed to be uncoupled, have significantly larger uncertainties than the equilibrium radiation properties. Instead of the 10 to 30% uncertainty seen for f_{ij} and $\Delta\lambda_S$ in Table 2, the nonequilibrium chemistry and non-Boltzmann rates have orders-of-magnitude uncertainties[1]. These large uncertainties are due mainly to a lack of experimental measurements at the high-temperature conditions of interest in a peak-radiative heating shock-layer. The presently studied EAST measurements therefore provide a valuable set of data for assessing the non-Boltzmann rate-model assembled by Johnston[1] and applied in HARA. These measurements may also be used to validate the quasi-steady state assumption[36] applied in the non-Boltzmann model's solution procedure, which allows the non-Boltzmann model to remain uncoupled from the flowfield model, as opposed to more complicated coupled approaches[37,38]. Furthermore, because the electron temperature and flowfield number densities obtained from the LAURA flowfield solver drive the non-Boltzmann model, these nonequilibrium data provide an opportunity to validate the thermochemical nonequilibrium models applied by LAURA.

The study of the 0.1 Torr data presented here will be similar to the study of the 0.3 Torr data presented in the previous section. The same multiplets presented in Table 2 and the same wavelength groupings presented in Tables 3 and 4 will be considered. However, the presence of significant regions of nonequilibrium and the fact the present cases are mostly optically-thin allow the discussion to focus on the nonequilibrium radiation (and the difference between the Boltzmann and non-Boltzmann models), instead of on the influence of line-widths and the optical-thickness on the equilibrium radiation, as was done for the 0.3 Torr cases.

A comparison between the measured and predicted intensity spectrum (J_λ) at 3.1 cm behind the shock is shown in Figure 12 for the 9.165 km/s case at 0.1 Torr (Case 3 in Table 1). The measured wavelength range for this case is 700 – 900 nm. In addition to the EAST data and present non-Boltzmann prediction, this figure also shows the result of increasing the shock velocity by 1.5% or by assuming a Boltzmann distribution of electronic states. It is seen that the baseline non-Boltzmann prediction under-predicts the data by nearly half. The significantly better prediction for the 1.5% increase in the shock velocity suggests that the 1.5% uncertainty is responsible for the present under-prediction of the measurements. The differences seen between the non-Boltzmann and Boltzmann predictions confirm the nonequilibrium state of the gas at this location.

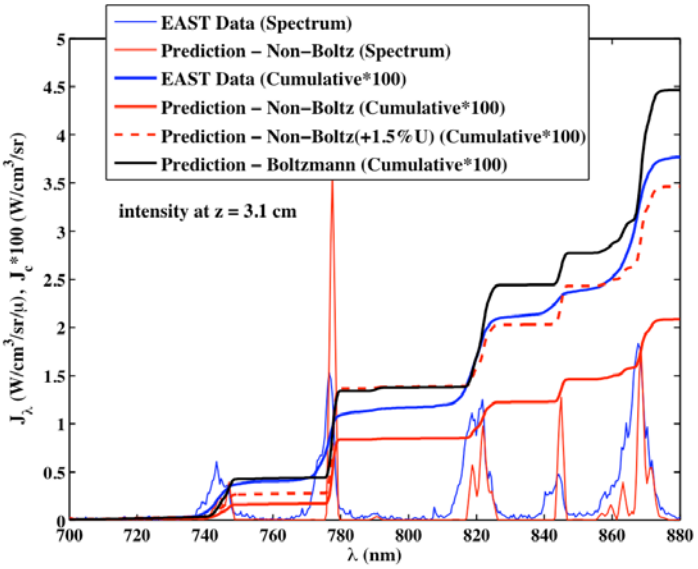

Figure 12. Comparison of the predicted and measured spectrum at z = 3.1 cm for Case 3.

Figures 13 and 14 compare the spatial variation of the integrated intensity over several spectral ranges for the measurement and predictions shown in Figure 12. The non-Boltzmann predictions for all of the spectral ranges except the 760 – 800 nm case are similar in shape but lower in magnitude than the measurements. Nitrogen atomic lines dominate these spectral ranges, while the 760 – 800 nm range is dominated by the 777 nm oxygen multiplet. The profile predicted for this oxygen multiplet range has a noticeably different shape than the measured profile. The nonequilibrium peaks for the Boltzmann predictions, which are cut off in the figures, reach $J_c x100$ values greater than 10 W/cm^3/sr. The non-Boltzmann predictions therefore agree much better with the measurements at these peaks. An important point to be made here is that measurements confirm the suppression of the significant Boltzmann-predicted emission, which is characteristic of the non-Boltzmann model in regions of nonequilibrium. Although the non—Boltzmann predicted nonequilibrium radiation is larger than the equilibrium radiation (which is approached near z = 4 cm) for these cases, the contribution of nonequilibrium radiation to the wall radiative flux for CEV is small because the length of the nonequilibrium region is roughly 2 cm along the stagnation-line, while the equilibrium region is roughly 15 cm. The Boltzmann predicted nonequilibrium radiation, on the other hand, is large enough in magnitude to contribute significantly to the wall radiative flux, even with the very small length of the nonequilibrium region. The experimental validation that the nonequilibrium radiation is closer to the non-Boltzmann prediction than the Boltzmann prediction is therefore valuable, because it confirms that the nonequilibrium radiation contribution is much less than that predicted by the Boltzmann model.

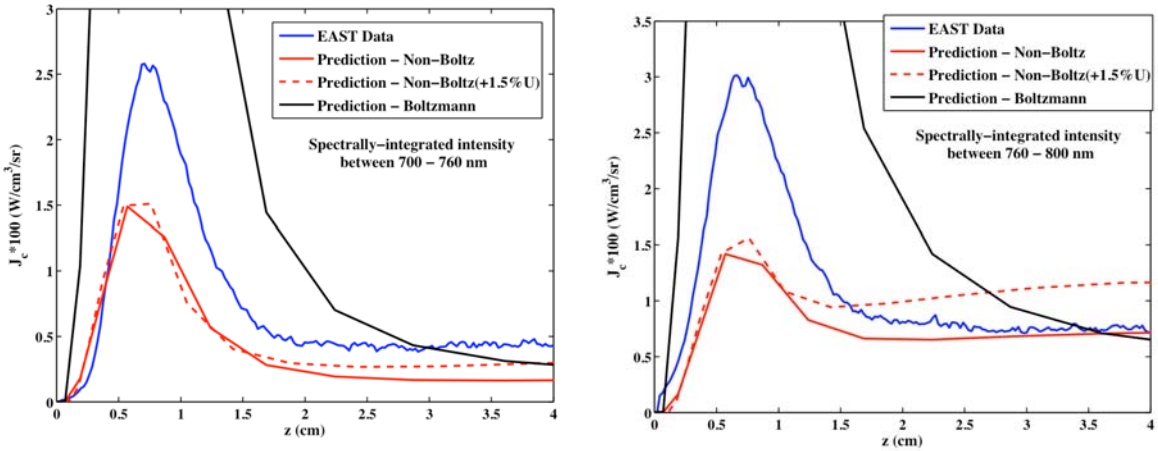

Figure 13. Spatial variation of the normalized intensity integrated over the 700-760 and 760-880 nm wavelength ranges for Case 3.

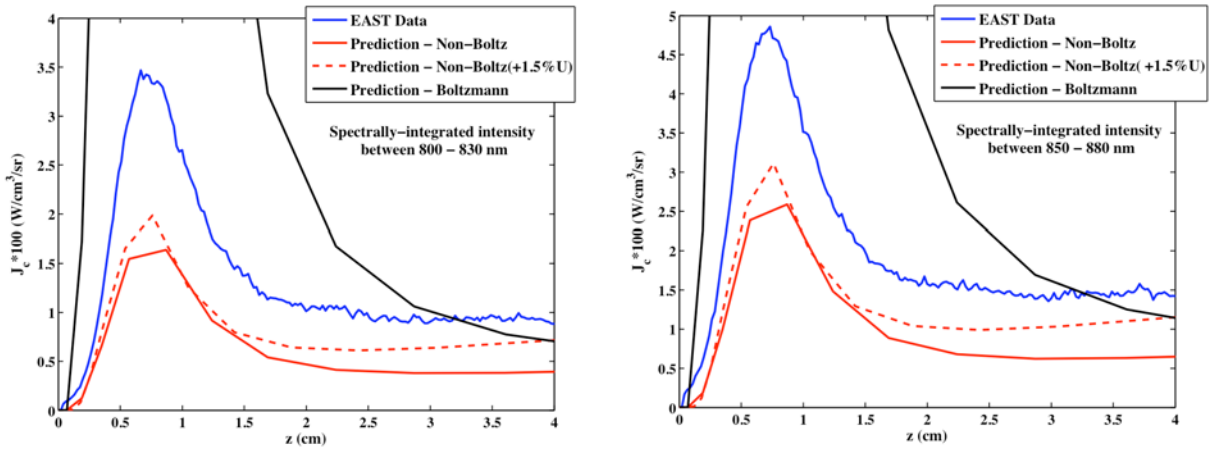

Figure 14. Spatial variation of the normalized intensity integrated over the 800-830 and 850-880 nm wavelength ranges for Case 3.

The measured and predicted intensity for the 9.989 km/s case at 0.1 Torr (Case 4 in Table 1) are compared in Figure 15. This comparison is made at z = 3.5 cm, with the measured spectral range spanning 900 – 1020 nm. The non-Boltzmann and Boltzmann predictions are coincident in this figure, indicating that the gas is in equilibrium at this z-location. Also notable in this figure is the agreement between the measurement and the prediction with a 1.5% increase in the shock velocity, which are seen to have nearly identical cumulative intensity curves.

The spatial variations of several spectrally integrated ranges are shown in Figures 16 and 17 for the measurement and predictions presented in Figure 15. The convergence of the Boltzmann and non-Boltzmann predictions at z = 3.5 cm indicates the approach to equilibrium. In the significantly nonequilibrium region between z = 0 and 2 cm, the non-Boltzmann predictions compare favorably with the measurements. While the 915 – 931 nm wavelength range is dominated by an oxygen multiplet, the other three wavelength ranges shown in Figures 16 and 17 are dominated by nitrogen multiplets. The prediction for the oxygen multiplet at 926 nm (multiplet 10 in Table 2) has a noticeably different profile shape than the nitrogen multiplets; the main difference being that the non-Boltzmann prediction for the oxygen multiplet reaches a slight peak at 2 cm, while the nitrogen multiplets do not reach any peak. This is similar to the behavior noted previously for the 777 nm oxygen multiplet. Note that the Boltzmann predictions for all cases in Figures 16 and 17 are similar and reach peaks ranging from 15 to 20 W/cm^2/sr.

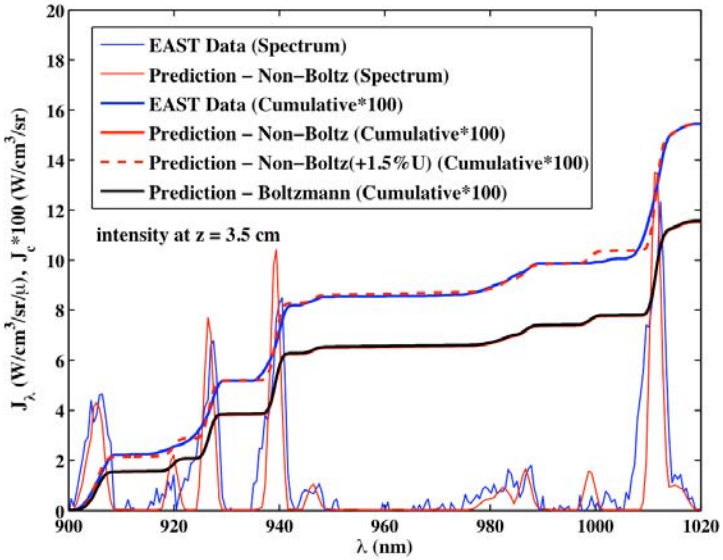

Figure 15. Comparison of the predicted and measured spectrum at z = 3.1 cm for Case 4.

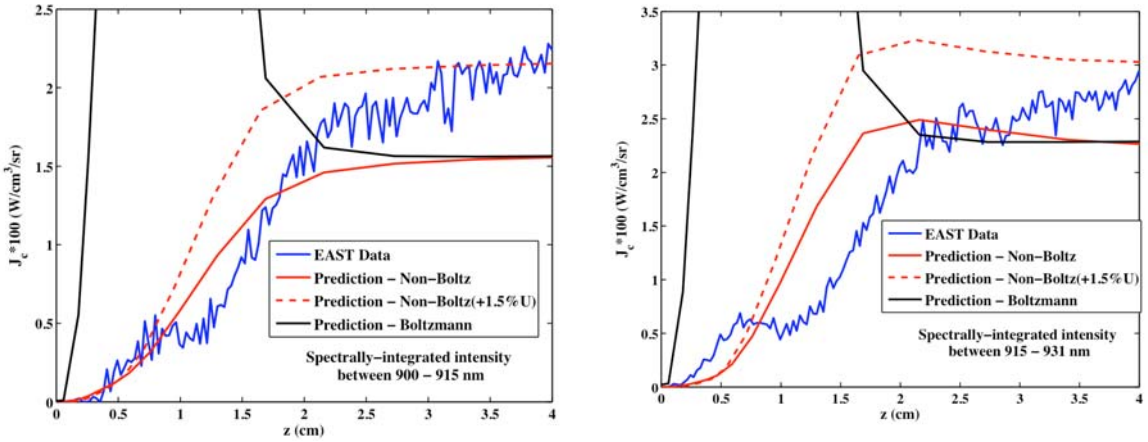

Figure 16. Spatial variation of the normalized intensity integrated over the 900-915 and 915-931 nm wavelength ranges for Case 4.

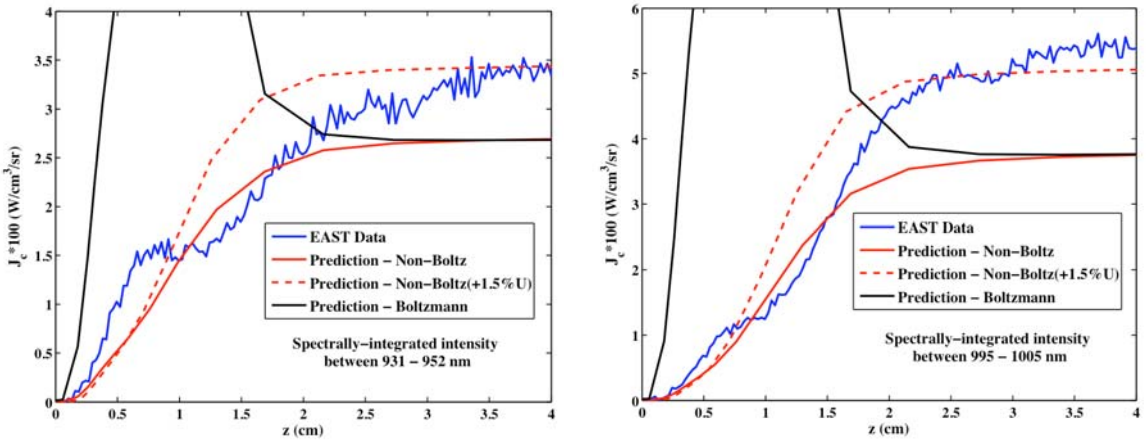

Figure 17. Spatial variation of the normalized intensity integrated over the 931-952 and 995-1005 nm wavelength ranges for Case 4.

To summarize the comparison with the 0.1 Torr data, Tables 5 and 6 present a detailed breakdown of Cases 3 and 4. The columns in these tables are similar to those in Tables 3 and 4. The column *j*, which was not in Tables 3 and 4, defines the upper level of the line transition. This is listed so that the results of the non-Boltzmann model, which calculates the population of these levels, may be related to the measured or predicted intensity from each line. The similar magnitudes of the j_{line} and J_{line} values in these tables confirm that the intensity is optically-thin for these cases. Consequently, the influence of a 10% increase in f_{ij} results in a nearly 10% increase in J_{total}, as indicated in the $\%\Delta J_{total}(f_{ij})$ column. The Stark broadening sensitivity, although not listed in these tables, is less than 1% for all cases. As mentioned previously, the percent differences between the predicted and measured value are improved significantly by applying a 1.5% increase in shock velocity for the predictions. This is seen in the tables by comparing the *%diff* column and the $\%\Delta J_{total}(U)$ column.

The column labeled $\%\Delta J_{total}(\Lambda)$ in Tables 5 and 6 lists the percent change in J_{total} when the non-Boltzmann model treats the vacuum ultraviolet (VUV) lines as optically-thin instead of optically-thick, meaning their escape factors (Λ) are set equal to zero instead of one[1]. This has the effect of depopulating the radiating levels, and therefore results in a decrease of J_{total}. It is clear from this table that the optically-thin assumption for the VUV lines degrades the comparison with the measurements (although note that the influence in Table 6 is much less than that in Table 5 because the electron number density is larger, meaning the electron-impact collisions dominate the non-Boltzmann model). This behavior is consistent with the fact that the VUV lines are not optically-thin, even though the lines in other spectral ranges are. Although they are rarely treated as such in a radiation transport calculation, the assumption is sometimes made in the non-Boltzmann modeling. This was done in the original version of HARA[1], which is why it is explicitly treated in this discussion. Note that the non-VUV escape factors are still assumed optically-thin in the non-Boltzmann model.

Table 5. Breakdown of measurements and predictions for Case 3 at z = 3.1 cm[a].

λ-range (nm)	Mult. ID#	λ_{CL} (nm)	j	j_{line} x100	J_{line} x100	J_{other} x100	J_{total} x100	J_{EAST} x100	% diff	$\%\Delta J_{total}$ (U)[b]	$\%\Delta J_{total}$ (f_{ij})[c]	$\%\Delta J_{total}$ (Λ)[d]
700-760	1	745.4	N10	0.13	0.14	0.03	0.17	0.4	140	61	7.8	-48
760-800	2	777.5	O6	0.73	0.67	0.01	0.68	0.76	12	64	8.5	-1
800-830	3	821.4	N9	0.35	0.35	0.03	0.38	0.94	148	69	8.8	-58
830-850	4	844.8	O7	0.25	0.22	0.01	0.23	0.27	13	75	9.0	-4
850-880	5	861.9	N12	0.12	0.11	0.02	0.62	1.49	124	67	9.0	-59
	6	869.4	N8	0.50	0.49							
							Total	=	80	67	8.7	-33
900-915	7	*905.2*	N16	.026	.025	.002	.043	-	-	109	9.5	-22
	8	*905.0*	N28	.016	.016							
915-931	9	*919.8*	N28	.011	.010	.002	.190	-	-	82	9.7	-3
	10	*926.6*	O10	.182	.178							
931-952	11	*939.7*	N11	.174	.172	.007	.179	-	-	67	9.0	-59
952-995	12	*983.3*	N20	.024	.023	.008	.031	-	-	86	7.4	-28
995-1005	13	*998.7*	N18	.004	.004	.001	.012	-	-	98	9.1	-31
	14	*999.1*	N19	.007	.007							
1005-1020	15	*1011*	N17	.135	.132	.003	.137	-	-	94	9.5	-36
							Total	=	-	83	9.3	-31

[a] $T_{tr} = T_{ve}$ = 8,282 K, N_N = 8.19e+16, N_O = 2.23e+16, N_e = 6.51e+14 particles/cm^3
[b] Percent change of J_{total} due to a 1.5% increase in the shock velocity.
[c] Percent change of J_{total} due to a 10% increase in all f_{ij} values.
[d] Percent change of J_{total} due to a assuming the VUV lines are optically thin in the non-Boltzmann model.

Table 6. Breakdown of measurements and predictions for Case 4 at z = 3.5 cm[a].

λ-range (nm)	Mult. ID#	λ_{CL} (nm)	j	j_{line} x100	J_{line} x100	J_{other} x100	J_{total} x100	J_{EAST} x100	% diff	$\%\Delta J_{total}$ (U)	$\%\Delta J_{total}$ (f_{ij})	$\%\Delta J_{total}$ (Λ)
700-760	1	745.4	N10	2.85	2.29	0.63	2.92	-	-	34	6.1	-7.4
760-800	2	777.5	O6	5.82	3.63	0.69	4.32	-	-	27	5.0	-1.0
800-830	3	821.4	N9	7.72	5.48	0.64	6.11	-	-	30	6.3	-5.6
830-850	4	844.8	O7	2.07	1.56	0.16	1.71	-	-	27	7.1	-17
850-880	5	861.9	N12	2.65	2.13	0.25	9.15	-	-	28	6.5	-6.5
	6	869.4	N8	10.7	6.77							
							Total	=	-	29	6.2	-6.1
900-915	7	*905.2*	N16	0.85	0.80	0.04	1.54	2.24	45	39	9.0	-0.7
	8	*905.0*	N28	0.74	0.70							
915-931	9	*919.8*	N28	0.50	0.49	0.09	2.25	2.94	31	34	9.1	-0.1
	10	*926.6*	O10	1.92	1.67							
931-952	11	*939.7*	N11	3.91	2.56	0.11	2.67	3.40	26	28	6.0	-4.1
952-995	12	*983.3*	N20	0.77	0.75	0.14	0.89	1.33	49	38	8.1	-5.7
995-1005	13	*998.7*	N18	0.14	0.14	0.03	0.38	0.20	-48	37	8.9	-6.3
	14	*999.1*	N19	0.22	0.21							
1005-1020	15	*1011*	N17	4.40	3.70	0.04	3.74	5.38	43	35	8.1	-3.2
							Total	=	34	34	7.9	-2.8

[a] $T_{tr} = T_{ve}$ = 9,621 K, N_N = 7.98e+16, N_O = 2.13e+16, N_e = 4.54e+15 particles/cm^3

The relative success of the present non-Boltzmann model in reproducing the measurements is seen in Figures 13 – 17 by comparing the non-Boltzmann prediction with the measurement and the Boltzmann prediction. In the very nonequilibrium 0 – 2 cm range, the non-Boltzmann model correctly suppresses much of the radiation predicted by the Boltzmann model, and predicts the nonequilibrium region shape and size to be consistent with the measurements. Further insight into this comparison is gained from inferring the number densities of the radiating levels from the measured intensities. This is achieved approximately with the following expression

$$N_j^{EAST} = \frac{J_{EAST} - J_{other}}{J_{total} - J_{other}} N_j \tag{12}$$

where J_{EAST}, J_{other}, and J_{total} are listed in Tables 5 and 6 and correspond to the spectral range containing the multiplet with an upper level j. Figure 18 compares the resulting number-densities for nitrogen resulting from Case 3. The left panel of Figure 18 corresponds to the z = 3.1 cm location, which was studied previously in Figure 12. The consistent under-prediction of the measurements is indicated by the under-population of the associated radiating levels. The similarity between the measurement and the Boltzmann prediction is shown in Figures 13 and 14 to be limited to the z = 3.1 cm spatial location. The right panel of Figure 18 corresponds to the highly nonequilibrium z = 0.65 cm location. A severely non-Boltzmann population distribution is predicted at this point, and is confirmed by the measurement-inferred values. Figure 19 presents the analogous distributions for Case 4. A fully equilibrium distribution is predicted for z = 3.5 cm, which is confirmed by the measurements. The strong nonequilibrium distribution at z = 1.0 cm is seen to be predicted relatively well. As indicated in Tables 5 and 6, these comparisons improve when a 1.5% increase in the shock velocity is accounted for. Although these values are not shown here, they would appear to shift the three predicted lines in each figure (Non-Boltz, Saha-Boltz, and Boltz) up slightly, while the inferred EAST data values would remain the same. The non-Boltzmann predictions obtained with an escape factor equal to one for the VUV lines, although also not shown, would lower only the non-Boltzmann curve, which would therefore worsen the comparison with measurements.

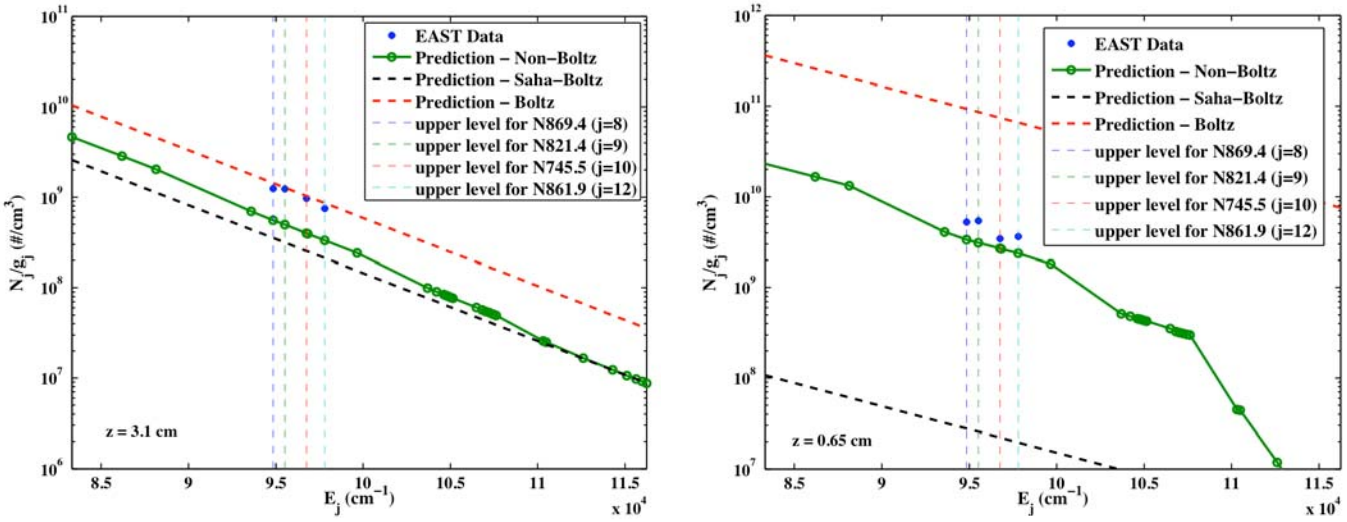

Figure 18. Population distributions for nitrogen resulting from predictions and those inferred from EAST measurements for Case 3.

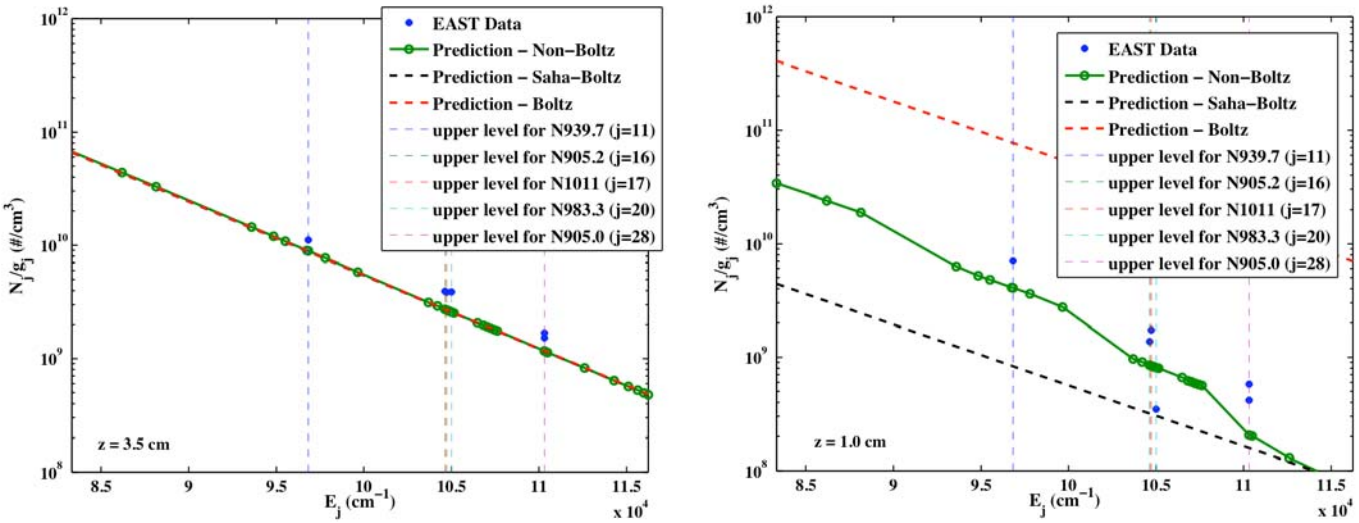

Figure 19. Population distributions for nitrogen resulting from predictions and those inferred from EAST measurements for Case 4.

VI. Molecular Band Emission in the 290 – 480 nm Wavelength Range

The 290 – 480 nm spectral range is distinctly different than the 700 – 900 and 900 – 1020 nm ranges studied in the previous two sections, because instead of being dominated by atomic lines, the 290 – 480 nm range is dominated by molecular band and atomic bound-free contributions. Furthermore, this spectral range is sensitive to carbon contamination because of strong emission from the CN violet band between 340 and 420 nm, which overlaps the strongly emitting N_2^+(1-) band system. Figure 20 shows the contributions from these two band systems, as predicted by the smeared rotational band model, for the thermochemical equilibrium region of Case 5. Also shown are the bound-free photoionization contributions from nitrogen and oxygen. Figure 21 compares the measured and predicted spectra for this case. The CN violet contribution is included by choosing a CN number density to fit the data, since CN is not included in the present chemistry model and the amount of contamination is unknown. A value of $7x10^{12}$ particles/cm^3 was chosen for the CN number density in this case. An important point in this comparison is that a constant value of 1.5 W/cm^3/sr/μ was subtracted from the experimental data, which reduces the experimental $J_c x100$ value by 28.5 W/cm^3/sr. As mentioned previously, the bound-free contributions in the 290 – 300 nm and 460 – 480 nm ranges are considered well known, and therefore there should be agreement between predictions and experiment in these regions. This subtracted component is interpreted as being a result of measurement calibration or flowfield contamination. It could also be interpreted as coming from a radiation mechanism in N or O that is not treated in the present model, such as the negative continuum[39]. This possibility requires further study.

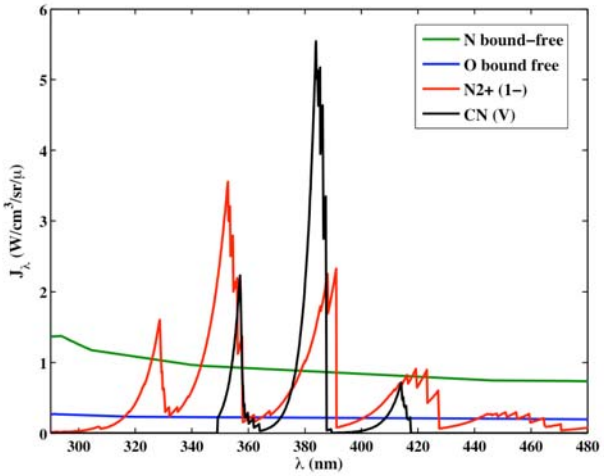

Figure 20. Components of the predicted spectrum, excluding atomic lines.

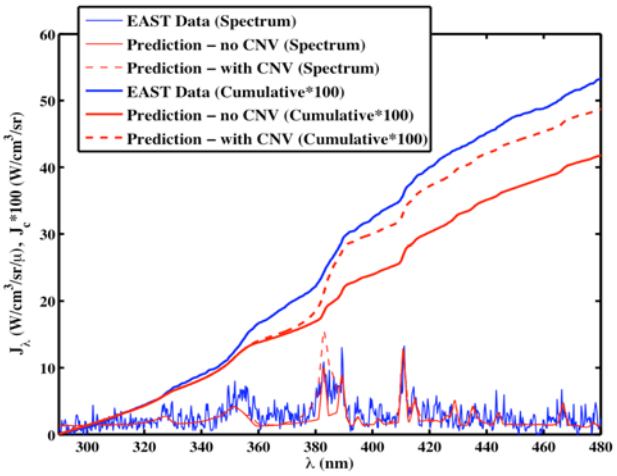

Figure 21. Experimental and predicted spectrum for Case 5.

The nonequilibrium emission in the 290 – 480 nm spectral range depends mostly on the behavior of the N_2^+(1-) and N_2(2+) band systems. The prediction of the nonequilibrium radiation from these bands requires the total molecular and electron number densities from the predicted LAURA flowfield and the non-Boltzmann excitation rates, which together are used to predict the number densities of the radiating N_2^+(B) and N_2(C) levels. For the present discussion, the excitation rates presented by Teulet et al.[40] are applied. For 0.1 Torr measurements of Case 6, Figure 22 shows the predicted and measured spectra at the peak nonequilibrium point, while Figure 23 shows the profile of the wavelength-integrated spectrum. These figures indicate the significant over-prediction resulting from the Teulet rate model. The results in these figures labeled "Reduced Teulet Rates" were obtained by dividing the Teulet rates for N_2^+ and N_2 by 70 and 10, respectively. The improved comparison in the nonequilibrium region due to these reduced rates indicates that the reduced rates are more appropriate when used in conjunction with the LAURA flowfield model. This does not necessarily mean that the physical processes are more accurately modeled by these reduced rates, because the present approach uncouples the non-Boltzmann calculation from the flowfield chemistry. Thus, they may be considered tuned to the present flowfield model. For both rate models, the predicted equilibrium radiation is significantly lower than the measurements. This is a result of the CN violet contamination, which is not considered in these nonequilibrium predictions.

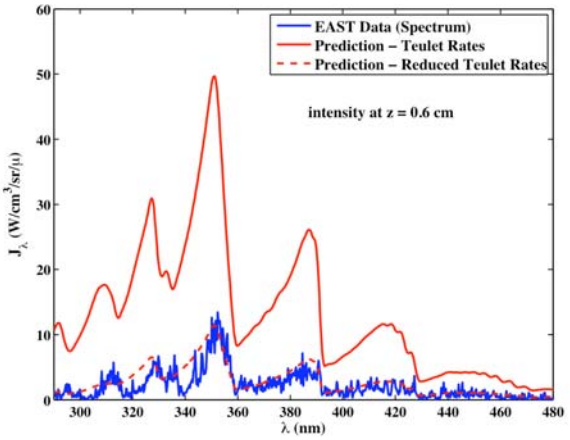

Figure 22. Predicted spectrum resulting from different excitation models compared with the measured spectrum at the peak nonequilibrium point (z = 0.6 cm) for Case 6.

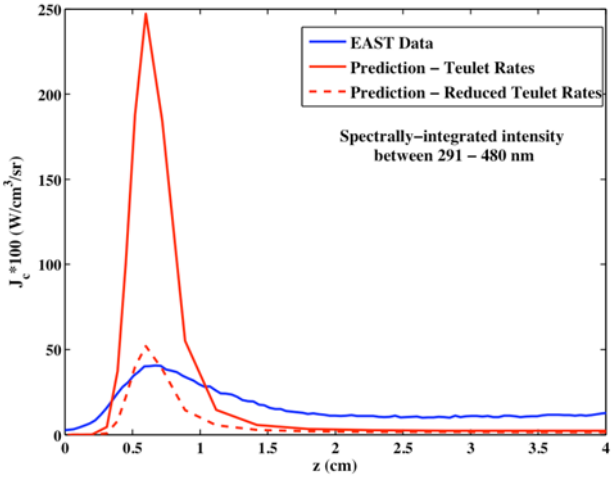

Figure 23. Profiles of the predicted and measured spectrally integrated intensity for Case 6.

VII. Conclusions

The equilibrium and nonequilibrium models applied in the HARA radiation code were assessed using the shock-tube radiation measurements of Grinstead et al.[23]. The thermochemical nonequilibrium post-shock flowfield was calculated using the LAURA code, and the nonequilibrium radiation was calculated using the HARA code. Spatial and spectral smearing was applied to the radiation predictions to make them consistent with the measured spatially and spectrally dependent radiation. The equilibrium radiation in the 700 – 1020 nm range, which contributes roughly 30% to a peak-heating lunar-return shock-layer, was shown to agree within 15% of the 0.3 Torr measurements. Accounting for the uncertainty of the measured shock velocity, the agreement was shown to be better than 15%. The sensitivity of the predictions to the oscillator strengths and Stark broadening half-widths were presented along with the published uncertainties for these data. The comparison of the measurements and predictions for the 0.1 Torr data validated the non-Boltzmann capability of the HARA code for atoms in the 700 – 1020 nm range. The treatment of the VUV lines as optically-thick in the non-Boltzmann modeling was shown to be necessary. Taking the shock velocity uncertainty into account, the predicted nonequilibrium radiation was shown to agree within 40% of the measurements. The molecular band and atomic photoionization radiation in the 290 – 480 nm range, which contributes roughly 8% to a peak-heating lunar-return shock-layer, were predicted well if a CN violet component was assumed due to carbon contamination, and if the non-Boltzmann rates for N_2 and N_2^+ were tuned to the data. Overall, the present comparisons with the measurements in the 700 – 1020 and 290 – 480 nm ranges provide the best validation of nonequilibrium shock-layer radiation available in the literature. Because the entire spectral range above 200 nm is characterized by the studied wavelength ranges, and since the majority of a peak-heating lunar return shock layer is in equilibrium, it is concluded from the *present interpretation* of the measurement and prediction comparisons that the radiative heating component *above 200 nm* (which accounts for roughly half of the total) may be predicted accurately within 15%.

References

[1] Johnston, C. O., *Nonequilibrium Shock-Layer Radiative Heating for Earth and Titan Entry*, Ph.D. Dissertation, Virginia Tech, November 2006.
[2] Park, C., "Nonequilibrium Air Radiation (NEQAIR) Program: User's Manual," NASA TM 86707, 1985.
[3] Nicolet, W.E., "Advanced Methods for Calculating Radiation Transport in Ablation-Product Contaminated Boundary Layers," NASA CR-1656, 1970.
[4] Wilson, K.H., "RATRAP – A Radiation Transport Code," Lockheed Report 6-77-67-12, 1967.
[5] Rigdon, W.S., Dirling, R.B., and Thomas, M., "Stagnation Point Heat Transfer During Hypervelocity Atmospheric Entry," NASA CR-1462, 1970.
[6] Cauchon, D.L., "Radiative Heating Results from the Fire II Flight Experiment at a Reentry Velocity of 11.4 Kilometers Per Second," NASA TM X-1402, July 1967.
[7] Johnston, C.O., "Nonequilibrium Stagnation-Line Radiative Heating for Fire II," AIAA Paper 2007-3908, 2007.

[8] Park, C., "Stagnation-Point Radiation for Apollo 4," *Journal of Thermophysics and Heat Transfer*, Vol. 18, 2004, pp. 349-357.
[9] Gruszczynski, J.S., and Warren, W.R., "Study of Equilibrium Air Total Radiation," *AIAA Journal*, Vol. 5, No. 3, 1967, pp. 517-525.
[10] Nerem, R.M., and Stickford, G.H., "Shock-Tube Studies of Equilibrium Air Radiation," *AIAA Journal*, Vol. 3, No. 6, 1965, pp. 1011-1018.
[11] Thomas, G.M., and Menard, W.A., "Measurements of the Continuum and Atomic Line Radiation from High-Temperature Air, *AIAA Journal*, Vol. 5, No. 12, 1967, pp. 2214-2223.
[12] Wood, A.D., Hoshizaki, H., Andrews, J.C., and Wilson, K.H., "Measurements of the Total Radiant Intensity of Air," *AIAA Journal*, Vol. 7, No. 1, 1969, pp. 130-138.
[13] Sutton, K., "Air Radiation Revisited," AIAA Paper 84-1733, 1984.
[14] Allen, R.A., Rose, P.H., and Camm, J.C., "Nonequilibrium and Equilibrium Radiation at Super-Satellite Re-Entry Velocities," AVCO Research Report 156, September 1962.
[15] Sharma, S.P., "Nonequilibrium and Equilibrium Shock Front Radiation Measurements," *Journal of Thermophysics and Heat Transfer*, Vol. 5, No. 3, 1991, pp. 257-265.
[16] Sharma, S.P., Assessment of Nonequilibrium Radiation Computation Methods for Hypersonic Flows," NASA TM-103994, 1993.
[17] Sharma, S.P., and Whiting, E.E., "Modeling of Nonequilibrium Radiation Phenomena: An Assessment," *Journal of Thermophysics and Heat Transfer*, Vol. 10, No. 3, 1996, pp. 385-396.
[18] Donohue, K., Reincecke, Rossi, D., Marinelli, W.J., Krech, R.H., and Caledonia, G.E., "Aerothermodynamic Radiation Studies," NASA CR-185666, 1991.
[19] Koreeda, J., Ohama, Y., and Honma, H., "Imaging Spectroscopy of the Nonequilibrium Shock Front Radiation in Air," *Shock Waves*, Vol. 8, No. 2, 1998, pp. 71-78.
[20] Morioka, T., Sakurai, N., Maeno, K., Honma, H., "Observation of Nonequilibrium Radiation behind Strong Shock Waves in Low-Density Air," *Journal of Visualization*, Vol. 3, No. 1, 2000, pp. 51-61.
[21] Fujita, K., Sato, Sunichi, S., Abe, T., and Ebinuma, Y., "Experimental Investigation of Air Radiation from Behind a Strong Shock Wave," *Journal of Thermophysics and Heat Transfer*, Vol. 16, No. 1, 2002, pp. 77-82,
[22] Matsuda, A., Fujita, K., Sato, S., and Abe, T., "Nonequilibrium Phenomena Behind Strong Shock Waves Generated in Superorbital Reentry Flight," *Journal of Thermophysics and Heat Transfer*, Vol. 18, No. 3, 2004, pp. 342-348.
[23] Grinstead, J., Wilder, M., Olejniczak, J., Bogdanoff, D., Allen, G., and Danf, K., "Shock-Heated Air Radiation Measurements at Lunar Return Conditions," AIAA Paper 2008-1244, 2008.
[24] Gnoffo, P.A., Gupta, R.N., and Shinn, J.L., "Conservation Equations and Physical Models for Hypersonic Air Flows in Thermal and Chemical Nonequilibrium," NASA TP-2867, 1989.
[25] Park, C., "Review of Chemical-Kinetic Problems of Future NASA Missions, I: Earth Entries," *Journal of Thermophysics and Heat Transfer*, Vol. 7, pp. 385-398, 1993.
[26] McBride, B.J., Zehe, M.J., and Gordon, S., "NASA Glenn Coefficients for Calculating Thermodynamic Properties of Individual Species," NASA TP 2002-211556, Sept. 2002
[27] Zeldovich, Y.B., and Raizer, Y.P., *Physics of Shock Waves and High Temperature Hydrodynamic Phenomena*, Vol. 1, Academic Press, New York and London, 1966.
[28] Hartung, L.C., "Predicting Radiative Heat Transfer in Thermochemical Nonequilibrium Flow Fields," NASA TM-4564, 1994.
[29] Wiese, W.L., Fuhr, J.R., and Deters, T.M., "Atomic Transition Probabilities of Carbon, Nitrogen, and Oxygen," *Journal of Physical and Chemical Reference Data Monograph*, No. 7, 1996.
[30] Konjevic, N., and Roberts, J.R., "A Critical Review of Stark Widths and Shifts of Spectral Lines from Non-Hydrogenic Atoms," *Journal of Physical and Chemical Reference Data*, Vol. 5, No. 2, 1976, pp. 209-252.
[31] Griem, H.R., *Spectral Line Broadening by Plasmas*, Academic Press, New York and London, 1974.
[32] Whiting, E.E., "An Empirical Approximation to the Voigt Profile," *Journal of Qualitative Spectroscopy and Radiative Transfer*, Vol. 8, 1968, pp. 1379-1384.
[33] Hartung, L.C., "Development of a Nonequilibrium Radiative Heating Prediction Method for Coupled Flowfield Solutions," *Journal of Thermophysics and Heat Transfer*, Vol. 6, 1992, pp. 618-625.
[34] Laux, C.O., "Optical Diagnostics and Radiative Emission of Air Plasmas," High Temperature Gas Dynamics Lab, Mechanical Engineering Dept., Rept. T-288, Stanford University, 1993.
[35] Johnston, C.O., Hollis, B.R., and Sutton, K., "Radiative Heating Methodology for the Huygens Probe," *Journal of Spacecraft and Rockets*, Vol. 44, No. 5, 2007, pp. 993-1002.
[36] Park, C., *Nonequilibrium Hypersonic Aerothermodynamics*, Wiley, New York, 1990.
[37] Bultel, A., Cheron, B.G., Bourdon, A., Motapon, O., and Schneider, I.F., "Collisional-Radiative Model in Air for Earth Re-Entry Problems," *Physics of Plasmas*, Vol. 13, 2006, 043502.
[38] Panesi, M., Magin, T.E., Bourdon, A., Bultel, A., Chazot, O., "Simulations of Nonequilibrium Reentry Air Plasmas by Means of a Collisional-Radiative Model," AIAA Paper 2007-4023, 2007.
[39] Chauveau, S., Deron, C., Perrin, M.-Y., Riviere, P., Soufiani, A., "Radiative Transfer in LTE Air Plasmas for Temperatures up to 15,00 K," *Journal of Qualitative Spectroscopy and Radiative Transfer*, Vol. 77, 2003, pp. 113-130.

[40] Teulet, P., Sarrette, J.P., and Gomes, A.M., "Calculation of Electron Impact Inelastic Cross Sections and Rate Coefficients for Diatomic Molecules: Application to Air Molecules," *Journal of Qualitative Spectroscopy and Radiative Transfer*, Vol. 62, 1999, pp. 549-569.